Structure of Water Adsorbed on Nanocrystalline Calcium Silicate Hydrate Determined from Neutron Scattering and Molecular Dynamics Simulations

Zhanar Zhakiyeva, Gabriel J. Cuello, Henry E. Fischer, Daniel T. Bowron, Catherine Dejoie, Valerie Magnin, Sylvain Campillo, Sarah Bureau, Agnieszka Poulain, Rogier Besselink, Stephane Gaboreau, Sylvain Grangeon, Francis Claret, Ian C. Bourg, Alexander E. S. Van Driessche, Alejandro Fernandez-Martinez

Corresponding Authors

Zhanar Zhakiyeva - University of Grenoble Alpes, University of Savoie Mont Blanc, CNRS, IRD, IFSTTAR, ISTerre, 38000 Grenoble; Institut Laue-Langevin, 38042 Grenoble, France; Department of Civil and Environmental Engineering, Princeton University, Princeton, New Jersey 08544, United States; Phone: +1(609)8993845; Email: zhanarz@princeton.edu

Gabriel J. Cuello - Institut Laue-Langevin, 38042 Grenoble, France; Phone: +33(0)476207697; Email: cuello@ill.eu

Alejandro Fernandez-Martinez – University of Grenoble Alpes, University of Savoie Mont Blanc, CNRS, IRD, IFSTTAR, ISTerre, 38000 Grenoble, France; Phone: +33(0)476635197; Email: alex.fernandez-martinez@univ-grenoble-alpes.fr

Ian C. Bourg – Department of Civil and Environmental Engineering and High Meadows Environmental Institute, Princeton University, Princeton, New Jersey 08544, United States; Email: bourg@princeton.edu

Alexander E. S. Van Driessche – University of Grenoble Alpes, University of Savoie Mont Blanc, CNRS, IRD, IFSTTAR, ISTerre, 38000 Grenoble, France; Email: alexander.van-driessche@univ-grenoble-alpes.fr

Authors

Henry E. Fischer – Institut Laue-Langevin, 38042 Grenoble, France;

Daniel T. Bowron – ISIS Facility, Rutherford Appleton Laboratory, Harwell Science and Innovation Campus, Didcot OX11 0QX, United Kingdom;

Catherine Dejoie – European Synchrotron Radiation Facility, 38000 Grenoble, France;

Valerie Magnin – University of Grenoble Alpes, University of Savoie Mont Blanc, CNRS, IRD, IFSTTAR, ISTerre, 38000 Grenoble;

Sylvain Campillo – University of Grenoble Alpes, University of Savoie Mont Blanc, CNRS, IRD, IFSTTAR, ISTerre, 38000 Grenoble;

Sarah Bureau – University of Grenoble Alpes, University of Savoie Mont Blanc, CNRS, IRD, IFSTTAR, ISTerre, 38000 Grenoble;

Agnieszka Poulain – University of Grenoble Alpes, University of Savoie Mont Blanc, CNRS, IRD, IFSTTAR, ISTerre, 38000 Grenoble;

36 *Rogier Besselink* – University of Grenoble Alpes, University of Savoie Mont Blanc, CNRS, IRD, IFSTTAR,

37 ISTerre, 38000 Grenoble;

38 *Stephane Gaboreau* – BRGM, Orléans Cedex 2 F-45060, France;

39 *Sylvain Grangeon* – BRGM, Orléans Cedex 2 F-45060, France;

40 *Francis Claret* – BRGM, Orléans Cedex 2 F-45060, France;

41 **ABSTRACT**

42 Calcium silicate hydrate (C-S-H) is a disordered, nanocrystalline material that acts as a primary

43 binding phase in Portland cement. Thin films of water are present on the surfaces and in nanopores of

44 C-S-H, impacting many of its chemical and mechanical properties, such as ion transport, creep, or

45 thermal behavior. Despite decades of research, a full understanding of the structural details of

46 adsorbed, confined, and bulk water in C-S-H remains elusive. In this work, we applied a multi-

47 technique study involving molecular dynamics (MD) simulations validated by neutron diffraction with

48 an isotopic substitution (NDIS) and X-ray scattering methods to investigate the structure of water in C-

49 S-H and C-A-S-H (an Al-bearing, low-CO_2 C-S-H substitute). Direct comparison of NDIS data with the

50 MD results reveals that the structure of confined and interfacial water differs significantly from the

51 bulk water and exhibits a larger degree of mesoscale ordering for more hydrated C-S-H structures.

52 This observation suggests an important role of water as a stabilizer of the atomistic-level structure of

53 C-S-H.

54 **1   INTRODUCTION**

55 Portland cement is one of the most important synthetic materials known to humans. In particular, it

56 plays a critical role in infrastructure and contributes a significant portion of anthropogenic CO_2

57 emissions.[1–4] Although its formulation has remained remarkably constant for decades, the

58 development of alternative formulations (low CO_2, CO_2 resistant, fire resistant, resistant to sulfate

59 attack, etc.) has emerged in recent years as an important research goal.[3,5–7] This new focus has

60 generated a strong need for detailed insight into the fundamental origins of the structural, mechanical,

61 and chemical properties of Portland cement. The task is challenging, however, because the structural

62 complexity of the hydrated Portland cement phase remains incompletely understood.

63 *The atomistic structure of C-S-H*

64 Calcium-silicate-hydrate (C-S-H), the main binding phase in Portland cement, is a nanocrystalline,

65 partially disordered, hydrated phase with water present in C-S-H pores of all sizes, from micro- to

66 meso- and macropores[6,8–10]. In addition to its structural disorder, C-S-H is also a complex material due

67 to its significant chemical versatility, in particular its variable Ca/Si ratio.[6,11,12] Since Taylor established

68 in 1950 the presence of two distinct phases with lower or higher Ca/Si ratios (C-S-H(I) and C-S-H(II),

respectively), there have been decades of debate about the structures of these phases.[13] It is now generally accepted that the structure of C-S-H(I) resembles a defective tobermorite, and that C-S-H(II) contains (nano)portlandite crystallites. Though questions remain regarding the spatial localization of the portlandite, a relatively unified view has emerged with many atomistic models available.[11,14–17] These different C-S-H models are consistently based on the structure of tobermorite, which consists of layers of calcium oxide sandwiched between silica chains formed by groups of three tetrahedra (dreierketten), with an interlayer space filled with water and ions.[15] These models differ primarily in their assumptions about the types of defects that exist in the tobermorite structure, with some common points regarding the substitution of Ca^{2+} ions by two hydroxyl groups and the presence of silica defects mainly in the 'bridging' tetrahedra of the 'dreierketten' silica chains.

In the last decade, a significant advance towards a more comprehensive understanding of C-S-H structure has been the application of atomistic simulation techniques to link C-S-H structural models to measured physical properties.[18] A milestone in C-S-H atomistic modeling was reached by Pellenq and coworkers with their development of a first C-S-H structural model with Ca/Si = 1.65, generated by creating defects in a tobermorite structure and then populating it with water molecules, using a Grand Canonical Monte Carlo (GCMC) approach.[19] Overall, the model reproduced several mechanical properties of C-S-H, such as stiffness, strength, and hydrolytic shear response, while deviating from measurements of certain structural features such as coordination numbers.[20] Qomi et al. later refined this model by using a "reactive" interatomic potential model (ReaxFF) to generate more chemically realistic structures and by creating a statistical ensemble of 150 atomic structures of C-S-H with varying Ca/Si ratios.[21] A similar approach was used by Kovačević et al.,[22] who also used a statistical approach to generate a large number of C-S-H structures with Ca/Si = 1.67 and with random numbers of silica oligomers for each model using both geometry optimizations and molecular dynamics (MD) simulations carried out with the ReaxFF force field. They showed that from an energetic point of view the model with Ca/Si = 1.67, achieved by randomly removing bridging silica tetrahedra and adding calcium ions charge-balanced by hydroxide ions, was the most stable structure. This also involved the breaking of silica chains into dimers and pentamers.[22,23]

More recently, an atomistic model that included a careful description and classification of different types of defects within the C-S-H structure was developed by Kunhi-Mohamed et al.[16] The authors created building blocks with varying defects to capture the disordered structure of C-S-H using a combination of density functional theory (DFT) and MD simulations. Their model reproduced the mean chain length (MCL) of C-S-H (based on experimental ^{29}Si NMR data) and its mass density. However, the authors reported that the predicted water content was significantly lower than expected and the interlayer spacing was quite large (2.5 Å higher than the expected value) for Ca/Si = 1.67.[16]

Finally, another recent atomistic model was proposed by Androniuk et al.[24] based on the structure of tobermorite, where defects were introduced only at the external surfaces, keeping the tobermorite bulk structure unchanged. [25] This model was used to study gluconate and U(VI) adsorption on C-S-H. [26] Deprotonated surface oxygens (which were assigned a more negative charge than structural oxygen atoms) were found to be the most favorable adsorption sites on the C-S-H surface, with a strong affinity for both Ca^{2+} and uranyl cations,[26] in agreement with their previous observation that the structural defects act as potential sorption sites for interfacial species.[25]

A key challenge in testing the validity of the structural models outlined above is that the X-ray diffraction pattern of C-S-H is composed of both Bragg peaks and diffuse scattering. This is indicative of a nanostructure containing some periodicity and a high degree of disorder. The presence of diffuse scattering makes the comparisons between experiments and calculations particularly challenging, albeit not impossible.[27] In recent years, experimental studies using Pair Distribution Function (PDF) analyses of high-energy X-ray scattering data have allowed a direct comparison of experimental and calculated PDFs. Unlike Bragg analysis (i.e., 'conventional' XRD analysis), the PDF approach allows the analysis of both short and long-range order. To date, few studies have directly compared predicted PDFs of C-S-H to experimental ones. Qomi[21] and Bauchy et al.[28] calculated X-ray PDFs from their simulation predictions and compared them to previously reported experimental PDFs of synthetic C-S-H.[29,30] The results showed good agreement with regard to the major peaks up to 5 Å, though some peak shifts or broadenings were observed. The most recent direct comparison was done by Cuesta et al.,[31] who compared their experimental data with calculated PDFs based on the model of Kunhi-Mohamed et al.,[32] showing an overall good agreement with some discrepancies in the middle-range order.[31,32]

Water in C-S-H

The models described above have contributed significantly to the advancement of our understanding of the defective structure of C-S-H and to the development of structure-properties relationships at the molecular scale. However, few of these models have addressed the structural properties of water films present at the C-S-H surface. It is well known that thin films of water adsorbed on metal oxides exert a strong control on many physico-chemical properties of the adsorbent phase, such as wettability, rheology, mechanical strength, and chemical reactivity (e.g., reactivity towards ions present within the interfacial liquid phase).[33–36] Studies of these interfacial liquid layers are thus of importance in cement chemistry and engineering. Indeed, these water films have been shown to strongly influence carbonation reactions,[37] cohesion,[38,39] shear strength,[40] and the deformation,[41] shrinkage[42] and creep behavior[43] of cementitious materials.

Since the early studies by Powers and Brownyard in 1948, who identified the so-called evaporable and non-evaporable water in the cement phase,[44] extensive effort has focused on characterizing the

different types of water in cement paste, and more specifically in the C-S-H phase. Different experimental techniques, including neutron scattering, have been used to probe the water component of C-S-H. In particular, Allen et al.[45] used small angle X-ray and neutron scattering to study the mesoscale arrangement of C-S-H nanoparticles. They concluded that C-S-H consisted of roughly 5 nm-wide platelets composed of stacked C-S-H layers with an interlayer space filled with water, and they distinguished between adsorbed water located on the surface of the platelets and a bulk-liquid-like water component located in the pores between these platelets.[45] Pinson et al.[46] proposed a similar classification of water based on the results of water sorption isotherms (WSI): they identified water confined in the interlayer space (≤ 1 nm), strongly bound to the C-S-H surfaces and removed only at relative humidities (RH) ≤ 11%; a "gel pore water" component in 1 to 10 nm wide pores; and capillary water in pores larger than 10 nm. Finally, they reported the presence of a surface layer of adsorbed water, which remained present in gel and capillary pores after the pores had been drained of bulk-liquid-like water.[46] Nuclear Magnetic Resonance (NMR), and in particular ^{1}H relaxometry experiments, have also provided detailed information on water dynamics in C-S-H and cement.[47] In particular, ^{1}H NMR relaxometry experiments by McDonald et al.[48] allowed differentiating between the mobile intra-C-S-H sheet water and inter-C-S-H gel pore water.[48] A few years later, Muller et al.[49] and Valori et al.[50] showed the potential of ^{1}H NMR relaxometry to distinguish between the dynamic characteristics of water in interlayer pores (< 1 nm), gel pores (2-5 nm), interhydrate pores (roughly 10 nm), and capillary pores (about 1000 nm). This subdivision of water in different pores and surfaces of C-S-H was subsequently studied by Roosz et al.,[51] who showed how an initially dry synthetic C-S-H sample behaves when exposed to increasing humidity. The authors proposed a two-step process, with water being adsorbed on the surfaces when humidity increases from 0 to 75% RH, and subsequently filling the mesopores and interlayer spaces as RH increases up to 95%.[51] These authors also showed that the process is not readily reversible, with interlayer water being released at much lower RH during water desorption.

Molecular mechanisms controlling C-S-H wettability

Even though, as shown above, the diffusive behavior of water in C-S-H has been the subject of multiple investigations, less information is available regarding the structural characteristics of the adsorbed water. Youssef et al.[52] used molecular modeling based on the structural C-S-H model of Pellenq et al.[19] to study water in confinement (interfacial/interlayer water). The authors showed with partial pair correlations of the water oxygen and hydrogen atoms that the local order of the confined water differed from that reported experimentally for bulk water.[53] The hydrophilic nature of C-S-H is explained by these authors as coming from the defective silicate chains, which act as hydrogen-bond (H-bond) acceptor sites, and from interlayer calcium ions, which coordinate water molecules.[52,54] This mechanism of surface hydrophilicity has been confirmed by studies on similar systems; for example,

5

172   Bonnaud et al.[39] showed using GCMC and MD methods that the hydrophilicity of Ca^{2+} ions physisorbed

173   in silica nanopores (a simplified model of C-S-H) decelerates the water dynamics as compared to the

174   hydroxylated silica surfaces without calcium ions. These authors also observed that the tetrahedral

175   arrangement of bulk water is disturbed near the hydrophilic surface, and perturbed much more in the

176   presence of calcium ions at the surface, due to water molecules being coordinated to Ca^{2+}.[39] As

177   discussed by Bourg and Steefel,[55] water within silica nanopores can be split into two types depending

178   on the pore size of the porous adsorbent: 2 to 20 nm wide pores contain significant amounts of surface

179   water (located in the ~3 first monolayers from the hydrophilic surface), which is highly structured and

180   different from the bulk-like water found in the center of the pores, while pores narrower than about 2

181   nm contain only confined water that is influenced by the two hydrophilic surfaces.[55] This simplified

182   model is representative of water in the C-S-H phase: the first type would correspond to gel-pore water,

183   with interfacial water (closest to the surface of C-S-H) having different structural characteristics than

184   the bulk-liquid-like water. The second type corresponds to interlayer water confined between two C-S-

185   H surfaces.[46] As a general trend, water near the surfaces of hydrophilic minerals tends to deviate more

186   from bulk-liquid-like water, both in terms of translational and orientational dynamics, and its

187   properties depend strongly on the nature of the substrate.[55–59] In the case of silica surfaces, the density

188   of surface hydroxyl groups dictates the wetting behavior, with a hydrophilic to hydrophobic transition

189   observed below 5 to 6 OH/nm^2.[21,60,61]

190   In this paper, the structural properties of interfacial and interlayer water in C-S-H are probed using a

191   combination of experimental and molecular modeling techniques. The technique of neutron diffraction

192   with isotopic substitution (NDIS) is used to probe the short-range order of water adsorbed on C-S-H

193   surfaces. [62,63] This method has previously been applied to systems showing structural similarities to C-

194   S-H, such as clay minerals. [64–66] To perform the molecular modeling simulations, a simple model of C-S-

195   H has been developed using a modified version of the CLAYFF force-field. Comparisons of the

196   calculated and experimental X-ray PDFs of C-S-H in the literature demonstrate the challenges

197   associated with creating an atomistic model that captures the complexity and disorder of the C-S-H

198   phase. One particular challenge in comparing these models with experimental results is that most

199   atomistic models developed for C-S-H (with very few exceptions)[67] share the similarity of being bulk

200   models (i.e., they are based on C-S-H structures that are infinite in at least two directions), whereas

201   experimental studies suggest that C-S-H is composed of nanocrystals with dimensions of only a few

202   nanometers.[30] The C-S-H model that we present in this work consists of a single particle with

203   dimensions of a few nanometers in every direction.

204   The paper is organized as follows: First, the stoichiometry of our experimental C-S-H samples and the

205   distribution of water as a function of RH are discussed. Then, the development of the C-S-H model is

206   described, including its validation by comparison to experimental scattering data. Finally, based on our

207 simulation and experimental results, we examine the structure and hydrogen-bonding (H-bonding)

208 behavior of interfacial and interlayer water in C-S-H and calcium-aluminum-silicate-hydrate (C-A-S-H)

209 samples conditioned at 55% and 98% of RH.

210 ## 2 MATERIALS AND METHODS

211 ### 2.1 Sample preparation

212 C-S-H samples with Ca/Si = 1 and 1.27 were synthesized by reacting calcium oxide and fumed silica in

213 water inside a N_2 wet glove-box. Calcium oxide was obtained by calcination of $CaCO_3$ (Sigma-Aldrich,

214 Fluka, Bioultra) at 1000 °C for 18 h and stored in a vacuum desiccator until usage. Fumed silica SiO_2

215 (Sigma-Aldrich, Aerosil 200) was placed in an oven at 40°C for 24 h to remove physisorbed water prior

216 to each experiment. Deionized water was boiled and degassed with N_2 gas to remove all dissolved CO_2.

217 The quantities of calcium oxide and fumed silica required to prepare C-S-H of predetermined

218 stoichiometry were calculated using the method reported by Haas and Nonat[68] (see Supporting

219 Information Table S3). Samples were reacted under stirring conditions for 1 month in High Density

220 Polyethylene (HDPE) bottles inside a wet N_2 glove-box, then filtered using Millipore® filter paper

221 (0.22 μm, GSW1 UM), and wet C-S-H residue was left to dry inside the glove-box for 12 h. A part of

222 these C-S-H samples was set aside for characterization of a fully-hydrated C-S-H. The remaining C-S-H

223 was oven-dried at 40 °C in a vacuum oven for 24 h. After drying, samples were conditioned at

224 controlled RH of 55 or 98 % using saturated salt solutions of $Mg(NO_3)_2 \cdot 6H_2O$ or K_2SO_4, respectively, in

225 duplicate with normal and deuterated water for 1 week (described schematically in Supporting

226 Information Figure S6). As samples are sensitive to atmospheric CO_2, all synthesis and conditioning

227 processes were performed under an inert gas atmosphere of N_2. The C-A-S-H samples with Ca/Si = 0.9

228 and 1.1 and Al/Si = 0.1 were synthesized following a protocol that can be found elsewhere.[17] The

229 conditioning time for the C-A-S-H samples was 1 month.

230 Following these protocols, we obtained C-S-H samples labeled CSH_Ca/Si_%RH_h/d, where Ca/Si is the

231 Ca/Si ratio of a sample, %RH is the relative humidity at which is was conditioned, and *h* or *d* signify

232 conditioning with normal or deuterated water (Table 1). The C-A-S-H samples were labeled

233 CASH_Ca/Si_%RH_h/d. In the discussion of the results of neutron diffraction with isotopic substitution

234 experiment (explained later), we refer to the difference between deuterated and hydrogenated

235 samples as CSH_Ca/Si_%RH_d-h, for example CSH_1_55RH_d-h. If the properties of the C-S-H samples

236 with a specific Ca/Si ratio are discussed in general, we refer to these as CSH_Ca/Si.

237 ### 2.2 Sample characterisation

238 **Inductively coupled plasma - atomic emission spectrometry (ICP-AES)**

239 Ca/Si ratios were determined using ICP-AES (Varian 720ES Agilent). The C-S-H particles (5-10 mg)

240 were dissolved by adding concentrated 14M HNO_3 (distilled) and 28M HF (47-51%, Trace Metal™, for

241 Trace Metal Analysis, Fisher Chemical) acids, followed by heating the solution for 24h at 80°C. The

242 final step involved diluting with boric acid and ultrapure water prior to the measurement.

Water adsorption volumetry

244 Water adsorption isotherms were obtained at 25 °C using a Belsorp-Max instrument by BEL JAPAN

245 Inc.III. A long acquisition time of at least 2 weeks was required due to the slow equilibrium kinetics.

246 Prior to the measurements, all samples were outgassed at 40 °C for 24 h under a residual pressure of

247 4.652×10^{-5} Pa. The classical Brunauer–Emmett–Teller (BET) theory and a generalized t-plot method

248 were used to analyze the isotherms.[69] The BET theory was employed to obtain energetic C constants,

249 which were used to plot t-curves based on the method discussed by Hagymassy[70] (Table 1).

Thermogravimetric analysis

251 Thermogravimetric analysis (TGA, Mettler-Toledo TGA-DSC3+) was used to examine the thermal

252 decomposition and the water content of the C-S-H and C-A-S-H samples. The samples were analyzed at

253 a heating rate of 10°C/min up to 600°C in a N_2 environment with a flow rate of 20 mL/min. The

254 samples were loaded in aluminum crucibles and were hermetically sealed with aluminum caps inside

255 a glove-box or a glove-bag filled with N_2 equilibrated at the same RH used to condition the sample. The

256 sample masses used for TGA analyses varied between 8 and 31 mg (20±2 mg for C-S-H with Ca/Si=1,

257 29±2 mg for C-S-H with Ca/Si=1.27, and 9±1 mg for C-A-S-H samples).

Attenuated Total Reflection Fourier-transform infrared (ATR-FTIR) spectrometry

259 FTIR spectra were acquired on an IS10 ThermoFischer spectrometer with high-performance diamond

260 ATR Smart iTX™ Accessory (IRSTEA, Grenoble). The different vibrational bands were assigned using

261 the OMNIC software.

Synchrotron X-Ray diffraction

263 Synchrotron XRD measurements for the C-S-H samples were performed at the ID31 and ID22

264 beamlines of the European Synchrotron Radiation Facility (ESRF) in Grenoble, France. Prior to

265 analysis, C-(A)-S-H samples were loaded into 1.5 mm (ID31) or 2 mm (ID22) polyimide capillaries in

266 glove-bags or a wet glove-box at the same RH values. The capillaries were closed on both ends using a

267 two-parts epoxy adhesive.

268 At the ID31 beamline, a monochromatic X-ray beam of 78 keV (λ = 0.159 Å) was used to obtain

269 scattering patterns of C-S-H with Ca/Si = 1. The data sets were collected using a PilatusX 2M CdTe

270 detector placed at a sample-to-detector distance of d_1 = 1.226 m to obtain scattering patterns with a Q

271 range of 0.1-6.2 Å^{-1}, allowing the measurement of the Bragg peak corresponding to the interlayer

distance of C-S-H. A second set of experiments was performed with a shorter sample-to-detector distance of $d_2 = 0.224$ m, yielding a Q range 0.6-27.6 $Å^{-1}$, for PDF analyses of the short- and medium-range order. C-S-H samples with Ca/Si = 1.27 were measured at the ID22 beamline with a monochromatic X-ray beam of 31 keV ($\lambda = 0.4$ Å). An angular range of 0.001-16° 2θ was used with a sample-to-detector distance of d = 1.4 m, corresponding to a Q range of 0.00027-4.37 $Å^{-1}$.

Data were automatically corrected for internal dark current. Two-dimensional images of the scattered intensity were azimuthally integrated using the pyFAI software package.[71] The pattern from the empty capillary was subtracted as a background. PDFs were obtained using the PDFGetX3 software.[72]

The C-A-S-H samples were measured at the 11-ID-B beamline at the Advanced Photon Source, Argonne National Laboratory. The samples were analyzed with a monochromatic X-ray beam of 58.6 keV (λ = 0.2115 Å). The data were collected with a Perkin Elmer XRD 1621 N ES detector and sample-to-detector distance of d = 0.799 m to access a Q range of 0.2-10.4 $Å^{-1}$. Data were automatically corrected for internal dark current. Two-dimensional images of the scattered intensity were azimuthally integrated using the GSAS II software package.[73]

2.3 Neutron diffraction with isotopic substitution

Neutron diffraction with isotopic substitution (NDIS) analyses (doi:10.5291/ILL-DATA.6-07-37, doi:10.5291/ILL-DATA.6-07-32) of C-S-H samples were performed at the D4 diffractometer[74] of the Institut Laue-Langevin (ILL), France. The incident wavelength of incoming neutrons was 0.4963 Å, as determined using a Ni powder reference. The samples were loaded in cylindrical (6.05 mm inner diameter, 6.35 mm outer diameter) vanadium containers sealed with a metallic O-ring under controlled atmospheres at the same RH values as the one used to condition the samples. The sample containers were weighed before and after each measurement to verify that no dehydration had occurred. Measurements were performed at ambient temperature (298 K). Results were corrected for inelasticity, multiple scattering, absorption, instrumental resolution, and background using the CORRECT program[75] and a custom-built Python code. Scattering and absorption cross sections were calculated using values from Sears' tables.[76] Scattering cross sections values for H and D were modified to account for 0.4963 Å neutrons or adsorbed and bulk pore water that lies outside the neutron beam's coherence volume. After the above-mentioned experimental corrections, the neutron structure factor S(Q) was obtained, which contains information about the structural organization of the material at the atomic level. Subsequent Fourier transformation of the S(Q) yielded the density function G(r), which is equivalent to the more commonly reported X-ray pair distribution function (PDF),[63] except for the difference in scattering lengths between neutrons and X-rays. Prior to calculation of the G(r), the total S(Q) was multiplied by a window function selected to reduce the effects of the limited momentum transfer range.[77]

NDIS experiments for the C-A-S-H samples were performed at the SANDALS diffractometer at the ISIS pulsed neutron source, United Kingdom. Experiments were performed at ambient temperature (298 K). The C-A-S-H samples were loaded in flat plate containers made of a "null scattering" alloy of Ti and Zr (35 mm x 35 mm x 2 mm) under controlled atmospheres at the same RH values as the ones used to condition the samples. The sample containers were weighed before and after each measurement to verify that no dehydration had occurred. The measurements used a neutron beam with wavelengths ranging from 0.05 to 4.95 Å, with a resulting Q range of 0.13 to 50 Å^{-1}. Results were corrected for inelasticity, multiple scattering, absorption, instrumental resolution, and background using the Gudrun package.[78]

Scattering patterns were obtained using samples conditioned with two different isotopes of H (^{1}H and D). Results were analyzed using the so-called first order difference method, by which all partial structure factors not involving H are cancelled out to obtain a partial structure factor centered on H (i.e. reflecting only the contributions of interatomic pairs involving at least one H atom). After Fourier transformation, the resulting G(r) is a partial pair distribution function centered on the H atom. [62,63] Prior to G(r) calculation, the total S(Q) was multiplied by a window function selected to reduce the effects of the limited momentum transfer range.[77] Additional information on the NDIS method is provided in the Supporting Information.

2.4 Molecular dynamics simulation

Atomistic simulations were performed at the Cori supercomputer at the National Energy Research Scientific Computing Center (NERSC, USA) using the MD simulation code LAMMPS,[79] which solves Newton's equations of motion for many-particle systems interacting through pairwise potentials. Interatomic interactions were described using the SPC water model[80] and the CLAYFF model of mineral-water interactions.[81] The CLAYFF force field was chosen because of its versatility and successful descriptions of various systems including clay minerals, [55,56,82–84] zeolites,[85] and other phases[86–88] validated against the results of X-ray and neutron scattering experiments [82,89] and a variety of other experimental techniques. [90,91]

A variety of force fields has been applied to simulate C-S-H and its crystalline analogues. These include the CLAYFF model, successfully applied to simulate a periodic C-S-H structure by Kalinichev and co-workers,[24,92] as well as a number of specialized force fields for cementitious systems, such as CSH-FF,[93] as summarized by Mishra et al.[94] One versatile option is the reactive force field ReaxFF[95], applied to C-S-H by several authors,[21,22,28,40] which can predict covalent bond dissociation and formation reactions. Unfortunately, comparison of ReaxFF simulation predictions with experimental microstructural data is complicated by its tendency to overestimate unit cell sizes, dissociation of the silica chains,[22] and the formation of silanol groups.[21,40] Finally, various studies have complemented the force field based

approaches outlined above using DFT methods, an approach that provides powerful fundamental insight but remains computationally costly for disordered systems such as C-S-H. [32,40]

In the present study, we have applied the CLAYFF force field to model, for the first time, a nanoparticle of C-S-H, including non-satisfied bonds at the edges in *x* and *y* directions. The modifications to the CLAYFF force field required to model the edge surfaces of C-S-H nanoparticles were performed based on the algorithms described in Lammers et al.[96]

Newton's equations of motion were solved using the Verlet algorithm with a 1 fs step. Electrostatic and dispersion interactions beyond a cut-off length of 15 Å were computed by Ewald summation. Water molecules were kept rigid using the SHAKE algorithm. The silica chains were kept semi-rigid by applying equilibrium bond angles θ_0 taken from the X-ray crystal structure of tobermorite,[97] with angle bending force constant K adapted from the INTERFACE force field of Heinz et al.[98] The C-S-H nanoparticle was fixed for the first 15 ps, during which only water molecules were allowed to move, after which all atoms were allowed to move. The system was equilibrated for 1.5 ns and, then, simulated for 3.5 ns production runs in the NVT ensemble at T = 298 K. Analyses of the MD simulation trajectories were performed using custom-made Python codes. Atomic structures were converted to PDFs using the DiffPy-CMI package[71] and averaged over multiple frames using a custom-made Python code. For the analysis of H-bonding structure, for simplicity, an H-bond was considered to exist if the intermolecular O-H distance was less than < 2.375 Å.[99]

2.5 C-S-H nanoparticle model construction

As a starting structure to build a C-S-H nanoparticle model we used the unit cell parameters and the atomic coordinates of the 14 Å tobermorite model by Bonaccorsi et al.[97] A supercell model was obtained by multiplication of the tobermorite unit cell in the x, y, and z directions. The bulk tobermorite supercell was then cleaved in the z direction along the plane of interlayer Ca ions (removing half of the exposed surface Ca ions), which created an uncharged basal surface identical to that examined in previous studies.[24] To construct a nanoparticle, the tobermorite structure was then cleaved in the x and y directions, which created surfaces referred to hereafter as the x and y edge surfaces (Figure 1).

To construct these x and y edge surfaces, Ca-O bonds were broken in the x direction and Si-O bonds were ruptured in the y direction. In order to ensure that the edges carried no under-coordinated metals (Si or Ca), in agreement with Pauling's bond-valence theory and with the original CLAYFF model, we used the algorithm developed by Lammers et al. [96] (The full list of parameters is reported in Table S2 in the Supporting Information.) This approach resulted in the definition of two oxygens types not listed in the CLAYFF model. The first is a *deprotonated* silanol (>SiO-) oxygen (Od, with charge q = -1.525 e), which has been previously used by authors to simulate clay edge surfaces and silica

surfaces.[100,101] The second is a *bridging edge* oxygen (Obe, with q=-1.2875 e), which is coordinated to one structural Si and one structural Ca atom. This bridging edge oxygen is found on the y edges and is under-coordinated by one structural Ca atom compared to CLAYFF bridging oxygen (Ob with q = -1.05 e).

A structure with a ratio of Ca/Si = 1 was then obtained by randomly removing bridging silica tetrahedra from our model tobermorite nanoparticle.[15] To maintain a charge-balanced structure, one of the bridging oxygens previously coordinated to the removed Si atom was replaced by a hydroxyl group, while the other was converted to a deprotonated silanol oxygen (See Supporting Information Figure S5). The resulting structure consists of silicate dimers and pentamers, which were shown to give energetically the most stable structures.[22,23] The lengths of these chains can be calculated using the Q^n definition describing different silicon environments identified by NMR: Q^1 are the species with one Si neighbour, and Q^2 have two Si neighbours. For this model, the ratio $Q^1/(Q^1+Q^2)$ is higher than generally reported for C-S-H with Ca/Si = 1 and closer to the value expected of Ca/Si = 1.2.[102,103] The reason for this too high number of Q^1 species may be the limited size of the nanoparticle, in which to achieve the Ca/Si = 1 the majority of bridging silicate tetrahedra had to be removed. Overall, we note that the precise structure of C-S-H remains unknown; therefore, we have tried to use the simplest C-S-H structure that was consistent with available information.
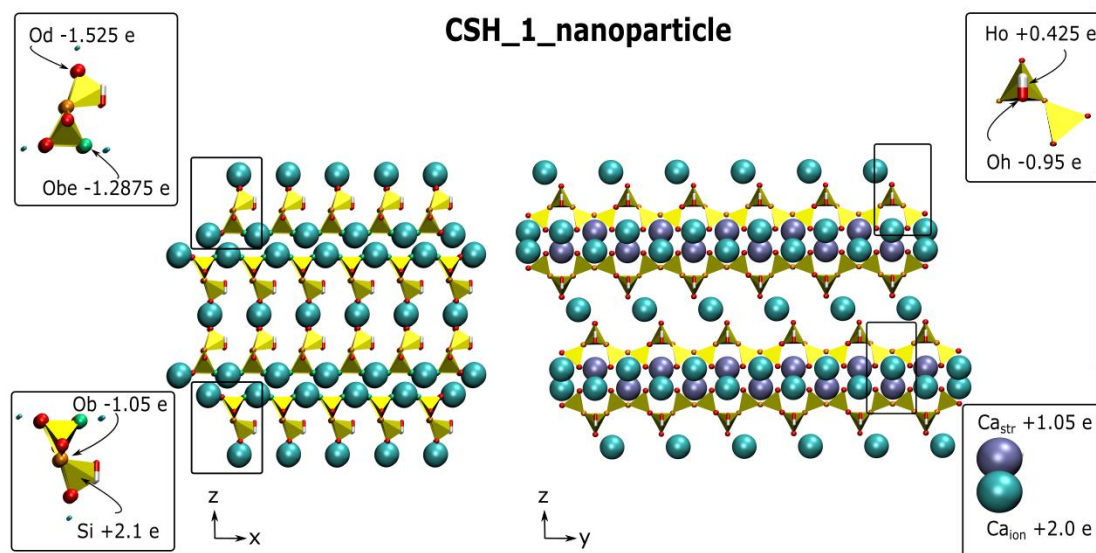
Figure 1. Idealized C-S-H nanoparticle structure (after the cleaving and healing of the external surfaces, but prior to the random removal of bridging silica tetrahedra) in x direction (left) and y direction (right) showing all the atom types: ionic calcium Ca_{ion} (turquoise spheres), structural calcium Ca_{str} (violet spheres), tetrahedral silica Si (yellow polyhedra), bridging oxygens Ob (orange dots), hydroxyl oxygens and hydrogens Oh and Ho (red and white licorice), bridging edge oxygens Obe (green dots), and deprotonated oxygens Od (red dots).

In this work, we simulated two models with two different hydration states. A high hydration state in which the 1892-atom C-S-H nanoparticle is suspended in a water droplet containing 12705 water molecules, which we named CSH_1_98RH, and a low hydration state where the particle is hydrated with only 448 water molecules, CSH_1_55RH. Thus, CSH_1_55RH model contains one monolayer of water, i.e. water within 3 Å from the C-S-H surface. In order to understand better the properties of the adsorbed interfacial water, we compared the first monolayer of water in CSH_1_98RH (referred later to as CSH_1_98RH_monolayer), with the water in CSH_1_55RH. The CSH_1_98RH_monolayer comprises about 1000 water molecules, which is roughly 2.2 times more than in CSH_1_55RH. These hydration states were selected to mimic the CSH_1_98RH_h (presence of bulk-liquid-like water, water to solid ratio 0.32 g/g) and CSH_1_55RH_h experimental systems (presence of only interfacial and interlayer water, water to solid ratio of 0.24 g/g). We emphasize that we refer to our simulated systems as 55RH or 98RH by analogy with the absence or presence of bulk-liquid-like water in our experimental conditions at these RH values, and that we did not quantify the activity of water in our simulations.

2.6 Stoichiometry of water in C-S-H

A precise determination of the stoichiometry and the types of water within the experimental samples is needed to analyze the NDIS data. Both bound water (i.e., water chemically incorporated into the structure of C-S-H) and so-called free water (i.e., water adsorbed on the surfaces and found in the capillary pores of C-S-H) are present in the samples and scatter neutrons differently. Therefore, a precise quantification of the abundance of structural hydroxyls, interlayer water, adsorbed interfacial, and bulk-like water in the capillary pores is paramount.

Calcium-silicate-hydrate has a highly variable stoichiometry, which mainly depends on the Ca/Si ratio and hydration state of the sample and is directly related to the abundance of defects in the C-S-H structure.[51,104–106] In our case, a key challenge was the estimation of the relative abundance of hydroxyls, interlayer water, interfacial water, and bulk pore water at varying RH values. Moreover, for a subset of our samples an additional complication arose from the incomplete deuteration of the deuterated C-S-H samples. To overcome this problem we applied the method described by Roosz et al.[51] and adapted it to the various RH values and deuteration levels of our samples.[51] The degrees of deuteration were obtained from ATR-FTIR spectra by comparing the relative areas under the O-H and O-D stretching frequencies at 3500 cm^{-1} and 2600 cm^{-1}, respectively (see Figure S3 in the Supporting Information). The total mass of water was obtained from the TGA measurements by assuming that at 300°C all the water in C-S-H had evaporated. Roosz et al.[51] used 150°C as a threshold value judging from the complete collapse of the interlayer spacing at this temperature by XRD. However, careful inspection of our data for C-S-H with various Ca/Si ratios and RH values revealed that 300°C is a more

appropriate threshold value to ensure that all bound water has evaporated. This value lies in the range of temperatures (260-600°C) in which a phase transition between tobermorite 14 Å and tobermorite 9.6 Å is observed, indicating the loss of highly bound water.[107] The remaining weight loss from 300°C-600°C was assumed to be due to the loss of hydroxyl groups, as portlandite dehydroxylation occurs around 450°C.[108] The maximum temperature was 600°C due to melting temperature of aluminum crucibles used. Roosz et al. noted that the temperature ranges used here are approximate and are sensitive to drying method and temperature.[51]

Adsorbed interfacial water content was quantified using the t-plot method, i.e., by plotting the volume of water adsorbed vs. the number of monolayers adsorbed at a certain value of RH. The specific surface area (SSA) and the volume of the monolayer $V_{monolayer}$ were derived from the BET equation. Then, the volume of water at a corresponding RH level was calculated by multiplying the statistical number of layers by $V_{monolayer}$. Interlayer water content was estimated by combining the values of the basal spacing (i.e., the d_{001} reflection) from the XRD data and the hysteresis observed by WSI (Table 1). Capillary bulk pore water content was calculated by subtracting the interlayer and adsorbed water masses from the total water mass. The same procedure was applied to the deuterated samples, taking into account the corresponding degrees of deuteration. The results of the above-described experiments and the stoichiometry for the C-(A)-S-H nanoparticles and the corresponding distribution of water are shown in Tables 1-2.

3 RESULTS AND DISCUSSION

3.1 Types of water and water content in C-S-H
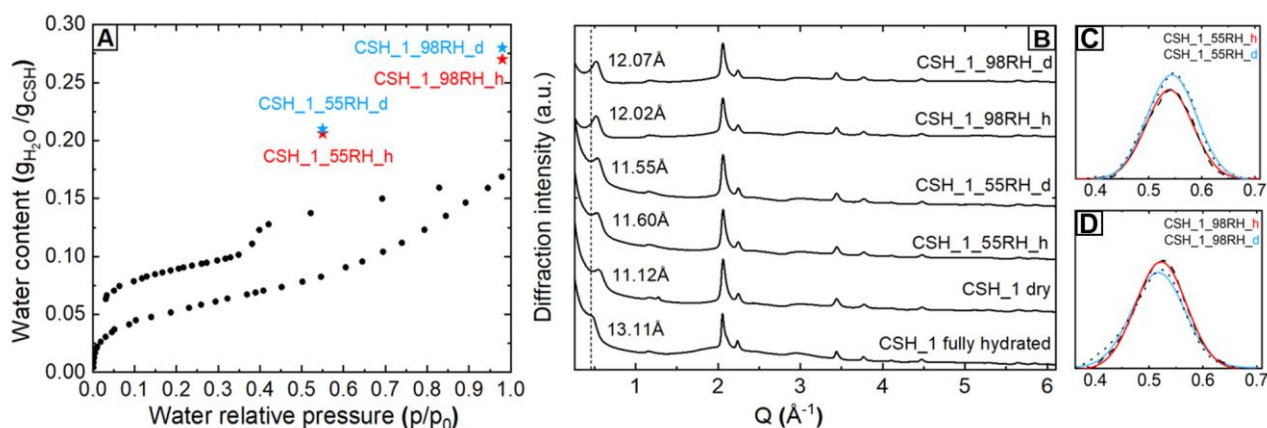
Figure 2. (A) Water adsorption/desorption isotherm of CSH_1. Black circles show WSI results. Red and blue stars indicate the water content deduced from the TGA data for hydrogenated and deuterated samples at 55 and 98% RH. (B) XRD patterns of CSH_1 fully hydrated (dried overnight in the glove-box), CSH_1 dry (oven dried at 40°C in vacuum), and hydrogenated and deuterated CSH_1 at 55 and 98% RH (conditioned for 1 week). The vertical dashed line shows the Q value associated with the d_{001} reflection of CSH_1 fully hydrated. (C,D) Examples of Pseudo-Voigt fits to the d_{001} reflection.

Adsorption/desorption isotherm for CSH_1 is shown in Figure 2 (other isotherms for C-(A)-S-H are shown in Figure S4 in the Supporting Information). In accordance with findings of Roosz et al.[51] and the IUPAC classification of Sing et al.[109] the isotherms belong to the type-II with H3 hysteresis loop behavior, signaling the presence of mesopores. The calculated BET SSA decreases with increasing Ca/Si ratios, from 187 m^2/g for CSH_1 to 132 m^2/g for CSH_1.27 (data for other Ca/Si ratios not shown here). The C-A-S-H samples follow a similar trend, with SSA values generally higher for C-A-S-H than for C-S-H (Table 1). The total amount of water derived from the TGA curves for CSH_1 samples is shown in Figure 2. Our TGA results for ~12 Ca/Si ratios at five different hydration levels (see Figure S8 in the Supporting Information) were compared to the data of Cong and Kirkpatrick[102] (and other authors[45,51,110–114]) and showed good agreement with the overall trend of increasing total H_2O/Si ratio with increasing Ca/Si ratio.

Both deuterated and hydrogenated C-(A)-S-H samples hold larger amounts of water as quantified by TGA than by WSI at the same RH values. One possible explanation is the limited equilibration time. The TGA samples were equilibrated in specific RH atmospheres by storing the C-S-H samples in desiccators over the saturated salt solutions for 1 week, and C-A-S-H samples for 1 month. The C-(A)-S-H samples measured with WSI were equilibrated for a few hours at each corresponding value of RH (done automatically by the instrument). Therefore, consistent with conclusions of Odler,[115] the amount of adsorbed water in the samples equilibrated for longer times (TGA experiment) is larger than in samples with shorter equilibration times (WSI experiment). Another potential difference is the normalization of the WSI points: Roosz et al.[51] normalized adsorbed water amounts by the mass of C-S-H dried at 150°C, estimated to correspond to fully dehydrated C-S-H, whereas we used the mass of C-S-H dried at 50°C, which is a an optimal pre-measurement sample degassing temperature.

As expected, the total mass of water is higher for the 98% RH samples than for the 55% RH samples, as the former contain capillary bulk water as well as interfacial and interlayer water. At 55% RH, samples contain 0.22 to 0.26 g water per g of dry C-S-H, as determined upon heating to 300°C, with the total mass of water decreasing slightly with increasing Ca/Si ratio. The abundance of hydroxyls is similar for all samples of same Ca/Si ratio (Table 2), and the difference in water content is due to varying RH levels.

Water release occurs at lower temperatures in the 98% RH samples, indicating the presence of more labile, bulk-liquid-like water. In TGA experiments the bulk-like water desorbs first, but the evaporation process can cause some partial migration/re-arrangement of the interfacial water, leading to shifts in the inflection points and to different shapes of dTG curves for 55% RH and 98% RH samples (Figure S2 in the Supporting Information).

492 ***Table 1.*** *Results of ICP, XRD, TGA, WSI, and ATR FT-IR experiments used to determine the stoichiometry*
493 *of C-(A)-S-H samples used in NDIS experiment.*

Sample name	ICP Ca/Si ratio	XRD d_{001} (Å)	Thermogravimetric analysis			Water sorption isotherms (BET method)			ATR FT-IR
			Mass loss (25-300 °C) (g/g_{dryCSH})	Mass loss (300-600°C) (g/g_{dryCSH})	Total mass loss (25-600°C) (g/g_{dryCSH})	BET c-value (-)	$V_{monolayer}$ (cm^3/g)	SSA_{BET} (m^2/g)	D/H ratio
CSH_1_55RH_h	1.04	11.6(1)	0.206	0.039	0.245	69	55	187	0.44
CSH_1_55RH_d		11.5(1)	0.21	0.047	0.257				
CSH_1_98RH_h		12.0(2)	0.27	0.05	0.32				21.4
CSH_1_98RH_d		12.1(2)	0.32	0.06	0.38				
CSH_1.27_55RH_h	1.27	10.3(1)	0.169	0.059	0.225	87	40	132	~0.5
CSH_1.27_55RH_d		10.3(1)	0.175	0.064	0.238				
CASH_0.9_55RH_h	0.9	12.4(2)	0.22	0.04	0.261	55	108	353	0.52
CASH_0.9_55RH_d		12.3(2)	0.24	0.045	0.285				
CASH_1.1_55RH_h	1.1	12.4(2)	0.207	0.039	0.246	67	90	291	~0.5
CASH_1.1_55RH_d		12.2(2)	0.216	0.05	0.266				

494 XRD patterns of C-S-H samples with varying water contents are shown in Figure 2. Results indicate
495 that the d_{001} spacing varies with Ca/Si ratio and RH level. The fully hydrated C-S-H has a full interlayer
496 space with d_{001} around 13.1(1) Å. Upon drying at 40°C in vacuum, the interlayer water evaporates and
497 the d_{001} value decreases to 11.1(1) Å. When these oven-dried samples were subjected to humid
498 atmospheres, interlayer water was partially reincorporated as reflected in the d_{001} values shown in
499 Table 1. The d_{001} reflection value and the total water contents derived from the TGA data were similar
500 for hydrogenated and deuterated samples at the same RH values, with slight differences possibly due
501 to the fitting errors of the XRD data and to the choice of temperature range (25 to 300 °C) used to
502 quantify water content from the TGA results. Moreover, the d_{001} reflection does not always uniquely
503 reflect the interlayer spacing, as d_{001} can be modulated by variations in scattering domain size[27] and

16

interstratification phenomena.[27,116] Nonetheless, previous studies have evidenced a trend towards decreasing d-spacing with increasing Ca/Si ratio,[15,27] with significant scatter hypothesized to result from differences in drying conditions, hydration levels, and sample handling.[51,116]

We note, in passing that the assigned stoichiometry of water in our samples may be, at least to some extent, unique to our dataset as the stoichiometry of water in C-(A)-S-H samples is sensitive to defect density (i.e., Ca/Si and Al/Si ratios), [6,106,117] drying method, [51,116] hydration level, [51,105] and sample handling (notably exposure to CO_2) in ways that remain incompletely understood.

Table 2. *Water stoichiometry in hydrogenated and deuterated C-(A)-S-H samples conditioned at 55% RH and 98% RH (more detailed stoichiometry in Supporting Information Table S1)*

Stoichiometry	Name	H_2O	D_2O
$Ca_1Si_1O_{2.8}(OH)_{0.4}$	CSH_1_55RH_h	1.32	
	CSH_1_55RH_d	0.99	0.42
	CSH_1_98RH_h	3.2	
	CSH_1_98RH_d		3.43
$Ca_1Si_{0.8}O_{2.43}(OH)_{0.59}$	CSH_1.27_55RH_h	0.93	
	CSH_1.27_55RH_d	0.58	0.47
$Ca_1Si_{1.1}Al_{0.11}O_{2.8}(OH)_{0.4}$	CASH_0.9_55RH_h	1.39	
	CASH_0.9_55RH_d	0.85	0.81
$Ca_1Si_{0.9}Al_{0.09}O_{2.63}(OH)_{0.45}$	CASH_1.1_55RH_h	1.45	
	CASH_1.1_55RH_d	0.55	0.71

3.2 C-S-H structure

In this section we present the C-S-H models and compare the results of the structural analysis with the experimental X-ray and neutron scattering data. The starting point of our model validation was to compare the experimental X-ray PDF data with the calculated PDFs derived from our MD simulation results (Figure 3).

17

529
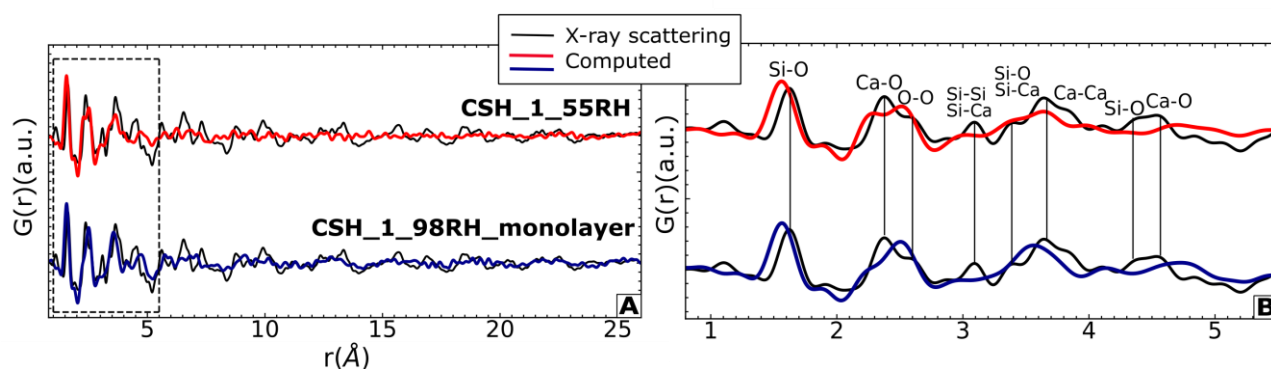
Figure 3. *(A) Experimental X-ray PDF of CSH_1_55RH (black lines) compared to the computed X-ray PDF for CSH_1_55RH (red line, top) and CSH_1_98RH_monolayer (darkblue line, bottom); (B) An enlarged region between 1-5.5 Å.*

The first observation after comparing the two calculated PDFs is that the CSH_1_98RH_monolayer is less disordered than the CSH_1_55RH structure. The calculated CSH_1_98RH_monolayer PDF broadly reproduces the overall shape of the peaks up to 30 Å, though the intensities of the predicted correlations are generally lower than those observed in the experimental data. The level of discrepancy with the experimental PDFs remains at an acceptable level, with the main peak distances reproduced (though with some shifts) as also reported by previous authors.[21,31,118]

A significantly lower degree of long-range structure is observed in the predicted PDF of the CSH_1_55RH sample, with no obvious correlations beyond 5.5-6 Å. This difference can be explained by the presence of an ordered interlayer space in CSH_1_98RH containing a full monolayer of water, which stabilizes the structure and prevents the C-S-H layers from collapsing into each other. This effect is clearly demonstrated by the difference between the atomic density profiles of structural calcium atoms of the two structures in the direction normal to the basal surface (Figure 4), where the results for CSH_1_55RH (Figure 4A) show that the layers are highly distorted. A possible explanation of this distortion may reside in the simplifications of the CLAYFF force field,[81] notably its reliance on fixed partial charges and its non-bonded representation of interatomic interactions within minerals. Our results suggest that reactive force fields, such as ReaxFF, where atomic charges are calculated at each simulation timestep, may enable a more realistic description of the transition from hydrated to dehydrated C-S-H interlayers.[95,119]

18
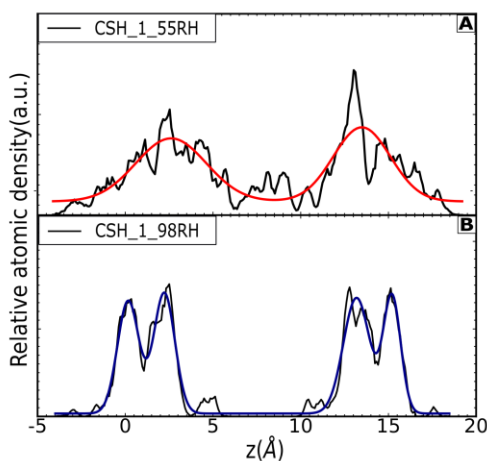
Figure 4. *Computed atomic density profiles of structural calcium atoms along the z direction for CSH_1_55RH (A) and CSH_1_98RH (B), with corresponding Gaussian fits in red and blue.*

Beyond the unexpectedly high structural distortion in the CSH_1_55RH system highlighted in Figure 4A, the interlayer distance calculated by fitting a Gaussian function through the structural calcium density profile yields a predicted basal spacing $d_{001\text{-}MD}$ = 11.0(2) Å, relatively close to the measured value of $d_{001\text{-}XRD}$ = 11.6(1) Å derived from the XRD measurements. In CSH_1_98RH (Figure 4B), the higher degree of interlayer hydration yields a larger basal spacing with excellent agreement between simulations and experiments ($d_{001\text{-}MD}$ = 13.0(2) Å vs. $d_{001\text{-}XRD}$ = 13.1(2), as reported in Table 1).

Comparison of X-ray PDF results over shorter distances (Figure 3B) shows that the two structures display similar short-range order. Experimentally, clear peaks are observed at 1.6 Å and 2.4 Å corresponding to Si-O and Ca-O correlations, respectively, followed by peaks at 3.1 Å (Si-Si and Si-Ca), 3.6 Å (Si-O and Si-Ca), 3.8 Å (Ca-Ca), and 4.3 Å (Si-O).[29] The calculated X-ray PDF data reproduce these correlations, with a slight shift for some of the peaks in both CSH_1_55RH and CSH_1_98RH_monolayer. The shifts in the first two peaks, corresponding to Si-O and Ca-O distances, can be directly attributed to a limitation of the CLAYFF potentials, as these distances derive directly from the force-field parameters. Another explanation for the Si-O distances differing from the experimental values could be the Si-O and Si-O-Si bond and angle parameters, which were adapted from the INTERFACE force field.[120]

570
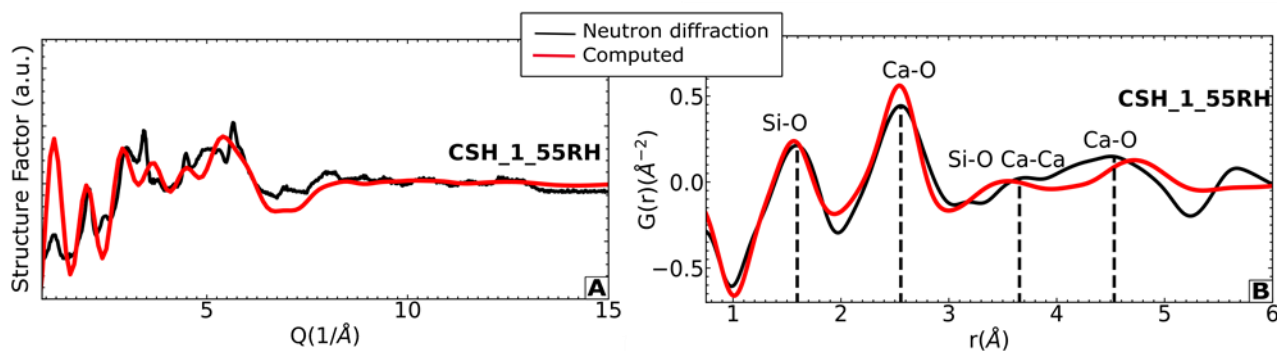
Figure 5. *(A) Total neutron structure factor and (B) total neutron G(r) of CSH_1_55RH_h showing the peaks corresponding to the atom pair correlations. Experimental data in black, computed data in red.*

The shifts in other peaks are likely due to the limitations of the C-S-H model: the size of the modeled nanoparticle is 44 Å at its longest side and the model clearly lacks crystallinity due to the high concentration of defects. Nonetheless, the main correlations up to 5 Å and their corresponding intensities are reasonably reproduced by the model.

 The next step in the model validation was to calculate the neutron scattering patterns, i.e., the total and partial S(Q) and G(r) functions (Figure 5). The calculated total structure factor of CSH_1_55RH (Figure 5A) reproduces the overall shape of the experimental S(Q), but the experimental C-S-H sample presents sharper Bragg peaks, a feature not captured by the calculated S(Q).

As stated above, this is probably due to the limited size of the coherent domain of our nanoparticle, which does not capture the long-range order that is present in some parts of the C-S-H samples. Still, the model reproduces satisfactorily the background oscillations from the diffuse scattering arising from the presence of water and the inherent disorder of the structure (Figure 5A).

Consideration of the total neutron G(r) confirms the broad consistency between experimental and computational results (Figure 5B). We note in passing that the experimental G(r), derived by a Fourier transformation of the structure factor, becomes unreliable at real-space correlation distances below 0.7 Å, as the scattered intensity was measured only up to a Q-range of 23.5 Å^{-1}.

3.3 Water structure

The Fourier transform of the first order difference S(Q) functions results in a partial $G_H(r)$, or partial PDF (Figure 6). The difference function represents the weighted sum of all the correlations functions involving hydrogen atoms. It is, therefore, much more sensitive to the structure of water than the results presented in the previous section. The neutron PDF functions in Figure 6 show overall similarities in the peak intensities and positions of the bulk capillary water in experimental

595 CSH_1_98RH_d-h and in the calculated PDF of CSH_1_98RH containing bulk water, shown in dark blue

596 (Figure 6B).

597
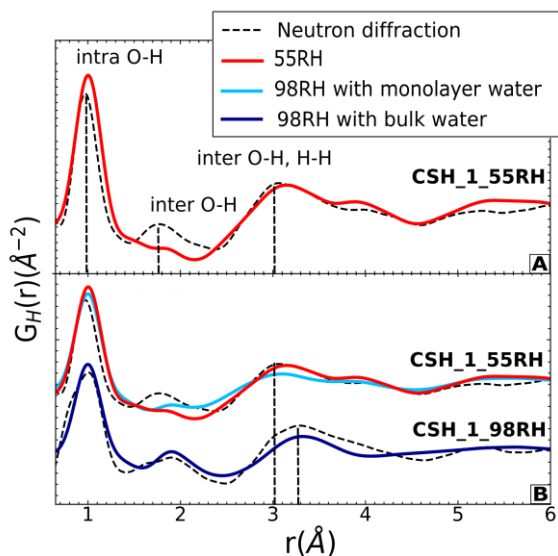
Figure 6. *(A) Partial neutron PDF of CSH_1_55RH_d-h and computed PDF CSH_1_55RH, showing the most*
significant atom correlations. (B) Partial neutron PDF of experimental (dashed black line) vs calculated
CSH_1_55RH (red line) and CSH_1_98RH with a monolayer of water (light blue line); experimental
(dashed black line) vs calculated CSH_1_98RH with bulk water (dark blue line)

602 The first peak at about 1 Å corresponds to the intra-molecular O-H distance. The second peak at 1.8 Å

603 corresponds to the intermolecular H-bonding. It is clear from Figure 6B that the position and intensity

604 of the intermolecular H-bonding peak is reproduced by the CSH_1_98RH model containing bulk water.

605 The red and light blue curves compare the short-range order of interfacial/interlayer water calculated

606 for the CSH_1_55RH system and for the CSH_1_98RH_monolayer (i.e., system CSH_1_98H considering

607 only interlayer water and the first monolayer of water on the external surfaces) against experimental

608 results obtained for CSH_1_55RH (dashed black line). The main difference between these curves is that

609 the intensity of the measured H-bonding peak of the CSH_1_55RH_d-h sample is underestimated by the

610 CSH_1_55RH model. Possible explanations for this discrepancy include model limitations as well as

611 potential differences in water content (i.e., the real 55RH sample may contain more water) and NDIS

612 data treatment artefacts associated with the Fourier transformation of the S(Q) to derive $G_H(r)$. A key

613 point of agreement of these curves, however, is in the peak at 3 Å. This peak results from

614 intermolecular correlations of the O-H and H-H atoms beyond the second nearest neighbor; therefore,

615 it reflects the structure of the H-bonded water network, rather than that of individual H-bonds

616 recorded by the peak at 1.8 Å. At this 3 Å peak, our results evidence a significant difference between

617 interfacial/interlayer and bulk-like water, with a shift in peak position from 3.3 Å (for bulk-liquid-like

618 water) to 3 Å (for interfacial/interlayer water) captured by both experimental and computational

619 results. In particular, the computed PDF of CSH_1_55RH captures both the intensity and the peak

position at 3 Å of experimental CSH_1_55RH_d-h, thus confirming that the 55% RH results probe interfacial/interlayer water. Further comparison with computed PDF of CSH_1_98RH_monolayer reveals that although the position and broadening of the H-bonding peak deviate somewhat from the CSH_1_55RH data, the position of the intermolecular O-H/H-H peak is within the 3 Å value. A comparison with the bulk-liquid-like water in CSH_1_98RH reveals a shift of this peak position to a value of 0.2 Å longer than for CSH_1_55RH. From this we can conclude that the local environment of the first monolayer of water on the surface of C-S-H is very similar to C-S-H containing only interfacial water. Likewise, the structure of water further than 1 monolayer from the surface resembles that of bulk liquid water.
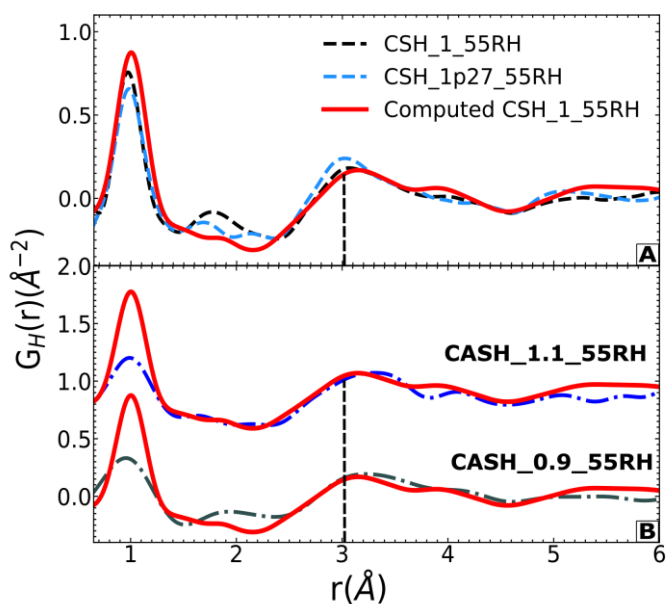
Figure 7. *(A) Partial neutron PDFs of the experimental CSH_1.27_55RH_d-h (dashed blue line) compared to experimental and computed CSH_1_55RH (red line). (B) Partial neutron PDFs of experimental CASH_0.9_55RH_d-h (dash dotted gray line) and CASH_1.1_55RH_d-h (dash dotted blue line) compared to the computed CSH_1_55RH.*

Comparison with NDIS results obtained for other samples reveals that the same features of the short-range order of water are found for the CSH_1.27 sample (Figure 7A) as well as for the C-A-S-H samples with Ca/Si = 0.9 and 1.1. The experimental C-A-S-H PDFs have lower peak intensities and broader peaks than the corresponding C-S-H PDFs (Figure 7B), likely because a smoothing window was required to compensate for the higher signal-to-noise ratio of the C-A-S-H data (particularly when extracting the difference signal between the deuterated and hydrogenated samples).

The similar local structure of interfacial/interlayer water in our C-A-S-H and C-S-H samples is consistent with a first-order approximation according to which the structure of C-A-S-H is similar to that obtained by substituting bridging Si by Al in C-S-H.[15] In our samples, one tenth of Si atoms were

643 substituted by Al, apparently with only limited effect on the structure of interfacial/interlayer water.
644 At higher Al/Si ratios, however, the structure of water in C-A-S-H may be different due to the increased
645 density of surface Ca ions required to charge balance structural Al.

646 Grangeon et al.[11] showed that the maximum Ca/Si ratio achievable by removing bridging silica
647 tetrahedra without precipitating portlandite is around 1.25.[11] Therefore, we suggest that the local
648 environment of water is dictated by the manner in which defects are introduced. Considering that in
649 CSH_1_55RH and CSH_1.27_55RH defects can be created by removing the bridging silica tetrahedra,
650 we presume that the structure of interfacial/interlayer water is similar for samples with these two
651 Ca/Si values. To achieve higher Ca/Si ratios it would be necessary to introduce calcium ions in the
652 interlayer or in the larger pores, leading to portlandite precipitation and, thus, probably creating a
653 different water environment.

654 Finally, deviations in interfacial/interlayer water structure relative to bulk water are shown by
655 comparing the Ow-Ow, Ow-Hw, and Hw-Hw pairs partial radial distribution functions of the calculated
656 bulk water, CSH_1_55RH, and CSH_1_98RH_monolayer structures (Figure S7 in Supporting
657 Information). Overall, there are clear differences between the partial RDFs of bulk water and
658 interfacial/interlayer water in our C-S-H models. The distance of the first Ow-Ow correlation of
659 interfacial/interlayer water is clearly shifted by ~0.2 Å with respect to that of the bulk water. The first
660 minima and the second peak are shifted from the bulk water by ~0.9 Å for CSH_1_98RH_monolayer
661 and by ~1 Å for CSH_1_55RH. In the Ow-Hw correlations the H-bonding peak at ~1.67 Å is lower than
662 in bulk water for CSH_1_55RH, and almost absent in CSH_1_98RH_monolayer. The Hw-Hw correlations
663 show the greatest deviations from bulk water, with the second peak almost absent and a much
664 broader and weaker third peak.

665 These findings are in agreement with the results of Youssef et al.[52], who showed that confined water
666 (interlayer and interfacial water) shows signs of distortion from the tetrahedral arrangement of bulk
667 water when confined between C-S-H layers. They proposed that the extended Ow-Ow correlations are
668 due to disordered hydrophilic C-S-H surfaces, with strong solvation effects of Ca ions and a quasi-two-
669 dimensional confining geometry of C-S-H surfaces.[52] Our results support this notion that the very
670 hydrophilic nature of C-S-H surfaces promotes a highly structured distribution of interfacial water.

671 **3.4 Distribution of interfacial and interlayer water on a C-S-H nanoparticle**

672 Predicted water distribution within our two C-S-H nanoparticulate systems, CSH_1_55RH and
673 CSH_1_98RH_monolayer, is shown in Figure 8. As mentioned above, a first qualitative assessment
674 reveals that the structure of the CSH_1_98RH model is less distorted than that of CSH_1_55RH. This
675 difference in crystallinity is observed at distances greater than 6 Å in the experimental PDFs (see
676 Figure 3). This is likely due to the fact that the interlayer space of CSH_1_98RH is filled with water

molecules, which have a stabilizing influence on the interlayer, affecting the crystallinity of the particle.[121] Although the structural distortion of our CSH_1_55RH model may reflect a limitation of the force field used here, another potential explanation is the small size and isolated nature of our model C-S-H nanoparticle. In real C-S-H samples, nanoparticles are agglomerated together within a larger solid matrix, which may help mitigate the stresses associated with sample drying.
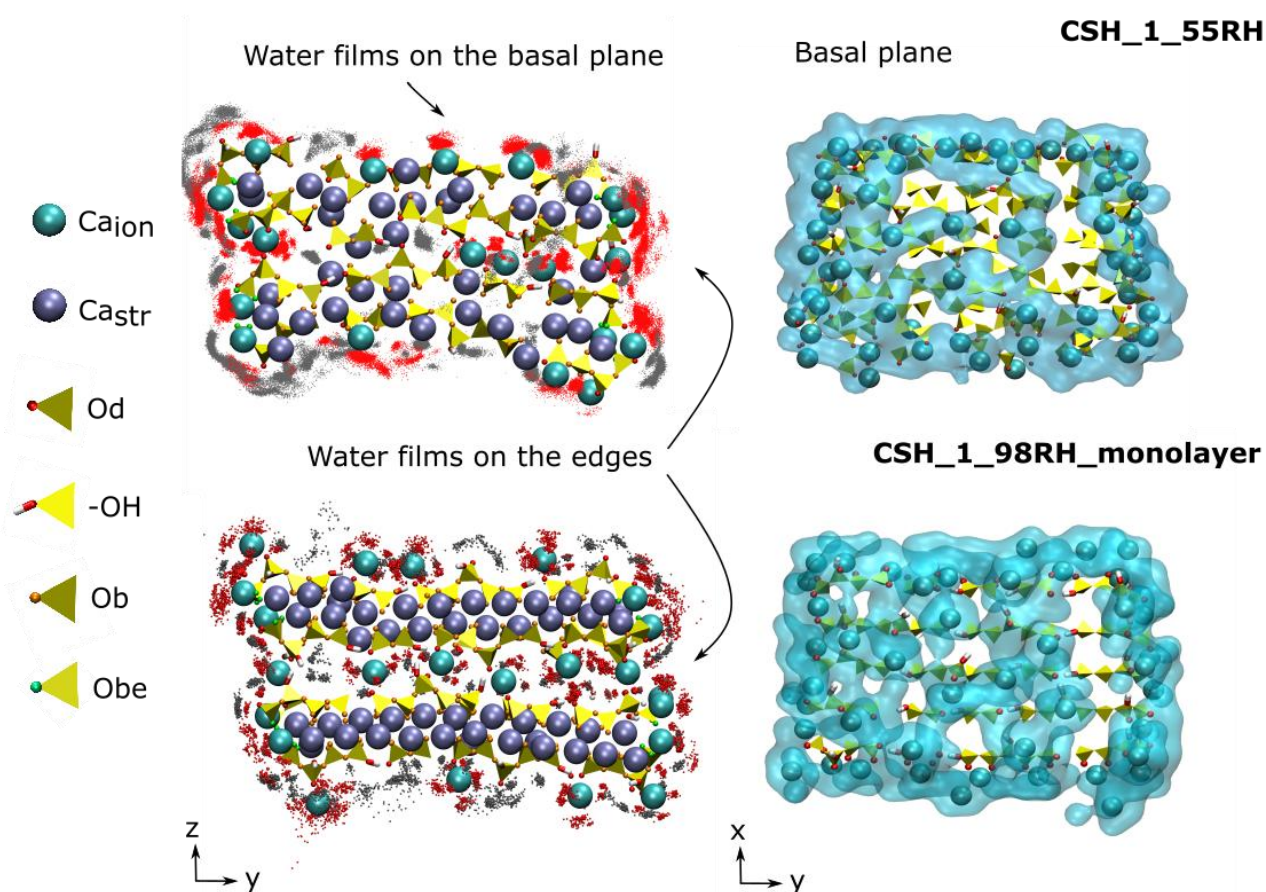
Figure 8. *(top left) Cross-section of CSH_1_55RH after 5 ns. Type I and type II water oxygens (red and grey dots, respectively) are shown as a cloud of coordinates sampled over a 5 ns trajectory. (bottom left) Same as the previous panel for CSH_1_98RH_monolayer sampled over 0.1 ns. Water forms thin films on the external surfaces and in the interlayer nanopore. (top and bottom right) Distribution of water on the upper external basal surface of the CSH_1_55RH and CSH_1_98RH nanoparticles. Water molecules (transparent blue surfaces) surround Ca^{2+} ions (turquoise spheres), confirming that these cations correspond to the most hydrophilic areas on the C-S-H surface.*

Indeed, whereas the diffuse scattering is well represented (see Figure 5A) in the calculated diffraction patterns for our C-S-H nanoparticle, these calculated patterns lack the Bragg peaks observed in the experimental patterns. This implies that the nanoparticle is probably too small to possess a coherent domain size able to reproduce the periodicity of the real sample. In small nanoparticles, the comparatively high importance of surface energy (vs. bulk energy) can result in significant structural relaxation,[122] as observed in our 55RH model. In this context, the greater distortion of the 55RH than

24

the 98RH model suggests more unfavorable interfacial energy at the lower hydration level, in agreement with almost twice lower coordination number of Ca^{2+} with water molecules, N_{Ca-H2O}, predicted for CSH_1_55RH than for CSH_1_98RH_monolayer (H_2O per Ca^{2+} 1.8 vs. 3.4, respectively).

Bearing in mind the above-mentioned differences in crystallinity between the two models, we now characterize the water distribution and H-bonding characteristics of interfacial and interlayer water. Due to the presence of highly negatively charged deprotonated surface oxygens (Od) and bridging edge oxygens (Obe), the surface of C-S-H is negatively charged. This controls the distribution of Ca^{2+} ions on the surfaces and in the interstitial cavities created by defects. In turn, these adsorbed Ca^{2+} ions are strong centers of charge that generate hydrophilic centers at the surface.[123–125] According to our simulations, most calcium ions are bonded to the deprotonated oxygen atoms at the surface, forming inner-sphere complexes, and they complete their coordination shell using water molecules. Therefore, for both CSH_1_55RH and CSH_1_98RH_monolayer, we discriminate between two types of water molecules on the C-S-H surface: (i) type I water molecules are those that coordinate surface Ca ions, while (ii) type II water includes all other interfacial/interlayer water molecules. Importantly, type I water molecules hardly accept any H-bonds, since the O atom of these molecules points towards the Ca^{2+} ion as shown by the results of neutron diffraction[126] and molecular orbital calculations.[123]

According to our simulations, in CSH_1_55RH, type I water represents 61% of the water in the sample, which is roughly 1.8 H_2O per Ca ion. The distribution of locations sampled by type I and type II water molecules during a 5 ns trajectory is highlighted in Figure 8 as red and grey dots, respectively. Both types of water predominantly form thin films on the basal and edge surfaces, representing 89% of the total water, with the remainder observed in the distorted interlayer. Type I water molecules donate the majority of H-bonds to deprotonated silanol oxygens (Od) and to water oxygens (Ow). The deprotonated oxygens receive about 0.5 H-bonds per Od with an average bond length (d) of 1.73 Å, and water oxygens receive roughly 0.3 H-bonds per Ow with d = 1.99 Å. Type II water molecules interact more strongly with deprotonated silanol oxygens (0.7 H-bonds accepted per Od with d = 1.66 Å) and less strongly with water oxygens (0.12 H-bonds received per Ow with d = 2.06 Å). Both types of water donate fewer H-bonds to the hydroxyl groups of surface silanols (0.2 H-bonds in total per Oh with d = 1.97 Å).

724
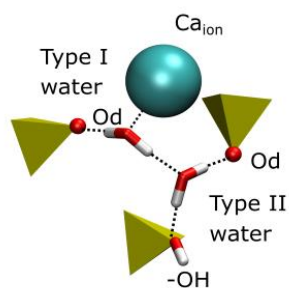
Figure 9. *Examples of some of the typical connections formed at the surfaces of the C-S-H nanoparticle. Ca ions (turquoise) coordinate type I water oxygens (red and white licorice), which donate H-bonds to deprotonated oxygens (red sphere) of surface silanols (yellow polyhedra) and to type II water molecules. The type II water molecules accept H-bonds from type I water molecules and donate H-bonds to deprotonated oxygens (red sphere) of surface silanols (yellow polyhedra) and to the oxygen (red and white licorice) of surface silanols (yellow polyhedra).*

The cross-section of CSH_1_98RH_monolayer reveals that the structure is much less distorted than that of CSH_1_55RH (Figure 8). The relative abundance of water in CSH_1_98RH allows the interlayer to be filled with water as seen by the interlayer spacing of about 13 Å (XRD value 13.1(2) Å for a fully hydrated C-S-H, Supporting Information Figure S1C).

The water molecules coordinated around calcium ions in the interlayer prevent the C-S-H layers from collapsing into each other (Figure 4). In this simulation, the amount of water present in the interlayer is 26% of the total. Hence, the ratio of interlayer water to interfacial water is roughly 2.5 times that of CSH_1_55RH. Not surprisingly, the larger share of the interlayer water affects the overall distribution and H-bonding behavior of water molecules in CSH_1_98RH. More precisely, in our CSH_1_98RH_monolayer, type I water comprises 53% of the total (i.e., about 530 out of 1000 water molecules found in the first monolayer from the C-S-H surface), so approximately 3.4 H_2O per Ca^{2+}. (Figure 8). As in CSH_1_55RH, type I water donates the majority of H-bonds to the surface of C-S-H and to other water molecules (Figure 9). However, it donates not only to Od (0.8 H-bonds received per Od with d = 1.68 Å), but also to the surface bridging oxygens Ob (0.2 H-bonds per Ob, d = 1.85 Å), and bridging edge oxygens Obe (0.2 H-bonds accepted per Obe, d = 1.91 Å). Type II water molecules donate a significant majority of H-bonds to the surface deprotonated oxygens Od, about 1.3 H-bonds per Od with d = 1.66 Å (Figure 9). The rest of H-bonds is shared between other water molecules (0.3 H-bonds received per Ow, d = 1.96 Å), and surface bridging oxygens (0.2 H-bonds per Ob, d = 1.86 Å) and hydroxyl oxygens (0.4 H-bonds per Oh atom, d = 1.95 Å). The latter is contrary to CSH_1_55RH, where silanol hydroxyl groups are quite hydrophobic. The reason is likely due to the abundance of water molecules in CSH_1_98RH, which provides more H-bonding opportunities and the possibility of creating an H-bonding network.

753 Overall, the interfacial water properties and structure are mostly similar in the partially hydrated
754 system (CSH_1_55RH) and in the first monolayer of the fully hydrated system
755 (CSH_1_98RH_monolayer). Observed differences in interfacial water structure in the two systems are
756 ascribed to the greater degree of Ca hydration, fully hydrated interlayer, and the presence of bulk
757 water in the fully hydrated system.

758 **4 CONCLUSION**

759 We have established an *in silico* nanoparticle model for C-S-H and validated it using experimental data.
760 This combined approach enabled us to study the properties of the different types of water present in
761 C-S-H conditioned at varying relative humidity values. We also compared our results to a low-CO_2
762 substitute for C-S-H, C-A-S-H. The results show consistent structural characteristics of water for the C-
763 S-H samples with the two Ca/Si ratios studied (1 and 1.27) as well as for the C-A-S-H samples. The
764 main mechanism for water adsorption is the coordination of water by hydrophilic Ca^{2+} ions, which
765 induces a strong H-bond network with other water molecules and with surface oxygen atoms. The
766 silanol groups play a minor role in this wettability mechanism: the C-S-H surface is characterized by a
767 combination of wet and dry regions, where wet areas are dominated by the presence of hydrophilic
768 calcium ions with strong hydration shells (Figure 8), whereas dry areas expose only silica chains and
769 silanol hydroxyls.

770 The results of the simulations show that the presence of water in C-S-H can have a strong influence on
771 the atomistic-level integrity of the layered structure. As shown in Figures 3 and 8, the more hydrated
772 structure shows a larger degree of mesoscale ordering, with a larger domain coherent size. This effect
773 could be due to the fact that the modelled C-S-H nanoparticle contained only two silicate layers, such
774 that the interactions of water molecules with the surface played a large role in the total intermolecular
775 interactions within the whole system. Similar results, where the water molecules exert a strong
776 influence on the bulk properties of inorganic nanoparticles, have been presented previously for other
777 systems.[127]

778 The wettability mechanism depicted here is susceptible to change at higher Ca/Si ratios, with the
779 formation of secondary portlandite. Whereas the exact location of the (nano)portlandite phase is still a
780 matter of discussion,[11] its presence and different surface structure could modify the overall structural
781 characteristics of the adsorbed water. Future experiments with samples containing higher Ca/Si ratios
782 should be performed to verify this hypothesis.

SUPPORTING INFORMATION

Neutron diffraction with isotopic substitution method theory, XRD, TGA, ATR FT-IR, and WSI results, water stoichiometry, creating defects in C-S-H model, MD parameters of the CSH_1_55RH and CSH_1_98RH model systems, example of partial charges calculations, synthesis amounts, synthesis and conditioning protocol, radial distribution functions for water, the total H_2O/Si vs Ca/Si.

REFERENCES

(1) Van Ruijven, B. J.; Van Vuuren, D. P.; Boskaljon, W.; Neelis, M. L.; Saygin, D.; Patel, M. K. Long-Term Model-Based Projections of Energy Use and CO_2 Emissions from the Global Steel and Cement Industries. *Resour. Conserv. Recycl.* **2016**, *112*, 15–36.

(2) Fischedick, M.; Roy, J.; Abdel-Aziz, A.; Acquaye, A.; Allwood, J.; Ceron, J.-P.; Geng, Y.; Kheshgi, H.; Lanza, A.; Perczyk, D.; et al. Industry. In *Climate Change 2014: Mitigation of Climate Change. Contribution of Working Group III to the Fifth Assessment Report of the Intergovernmental Panel on Climate Change*; Cambridge University Press: Cambridge, U.K., New York, NY, USA., 2014. https://www.ipcc.ch/site/assets/uploads/2018/02/ipcc_wg3_ar5_frontmatter.pdf (accessed 2020-03-15).

(3) Lehne, J.; Preston, F. *Making Concrete Change Innovation in Low-Carbon Cement and Concrete.* Chatham House Report; London, U.K., 2018. https://www.chathamhouse.org/sites/default/files/publications/research/2018-06-13-making-concrete-change-cement-lehne-preston.pdf (accessed 2020-07-27).

(4) CEMBUREAU. *Cementing the European Green Deal, Reaching Climate Neutrality along the Cement and Concrete Value Chain by 2050,* 2020. https://cembureau.eu/media/kuxd32gi/cembureau-2050-roadmap_final-version_web.pdf (accessed 2020-07-02).

819 (5) Van Damme, H. Concrete Material Science: Past, Present, and Future Innovations. *Cem. Concr.*
820   *Res.* **2018**, *112*, 5–24.

821 (6) Lothenbach, B.; Nonat, A. Calcium Silicate Hydrates: Solid and Liquid Phase Composition. *Cem.*
822   *Concr. Res.* **2015**, *78*, 57–70.

823 (7) Scrivener, K. L.; Kirkpatrick, R. J. Innovation in Use and Research on Cementitious Material. *Cem.*
824   *Concr. Res.* **2008**, *38*, 128–136.

825 (8) Skalny, J.; Odler, I. Pore Structure of Calcium Silicate Hydrates. *Cem. Concr. Res.* **1972**, *2*, 387–
826   400.

827 (9) Papatzani, S.; Paine, K.; Calabria-Holley, J. A Comprehensive Review of the Models on the
828   Nanostructure of Calcium Silicate Hydrates. *Constr. Build. Mater.* **2015**, *74*, 219–234.

829 (10) Wenzel, O.; Schwotzer, M.; Müller, E.; Chakravadhanula, V. S. K.; Scherer, T.; Gerdes, A.
830   Investigating the Pore Structure of the Calcium Silicate Hydrate Phase. *Mater. Charact.* **2017**,
831   *133*, 133–137.

832 (11) Grangeon, S.; Fernandez-Martinez, A.; Baronnet, A.; Marty, N.; Poulain, A.; Elkaïm, E.; Roosz, C.;
833   Gaboreau, S.; Henocq, P.; Claret, F. Quantitative X-Ray Pair Distribution Function Analysis of
834   Nanocrystalline Calcium Silicate Hydrates: A Contribution to the Understanding of Cement
835   Chemistry. *J. Appl. Crystallogr.* **2017**, *50*, 14–21.

836 (12) Chen, J. J.; Thomas, J. J.; Taylor, H. F. W.; Jennings, H. M. Solubility and Structure of Calcium
837   Silicate Hydrate. *Cem. Concr. Res.* **2004**, *34*, 1499–1519.

838 (13) Taylor, H. F. W. Hydrated Calcium Silicates. Part I. Compound Formation at Ordinary
839   Temperatures. *J. Chem. Soc.* **1950**, 3682–3690.

840 (14) Richardson, I. G.; Groves, G. W. Microstructure and Microanalysis of Hardened Cement Pastes
841   Involving Ground Granulated Blast-Furnace Slag. *J. Mater. Sci.* **1992**, *27*, 6204–6212.

842 (15) Richardson, I. G. Model Structures for C-(A)-S-H(I). *Acta Crystallogr. Sect. B Struct. Sci. Cryst. Eng.*
843   *Mater.* **2014**, *70*, 903–923.

844 (16) Kunhi Mohamed, A.; Parker, S. C.; Bowen, P.; Galmarini, S. An Atomistic Building Block
845   Description of C-S-H - Towards a Realistic C-S-H Model. *Cem. Concr. Res.* **2018**, *107*, 221–235.

846 (17) Roosz, C.; Vieillard, P.; Blanc, P.; Gaboreau, S.; Gailhanou, H.; Braithwaite, D.; Montouillout, V.;
847   Denoyel, R.; Henocq, P.; Madé, B. Thermodynamic Properties of C-S-H, C-A-S-H and M-S-H
848   Phases: Results from Direct Measurements and Predictive Modelling. *Appl. Geochemistry* **2018**,
849   *92*, 140–156.

850 (18) Faucon, P.; Delaye, J. M.; Virlet, J.; Jacquinot, J. F.; Adenot, F. Study of the Structural Properties of
851   the C-S-H(I) by Molecular Dynamics Simulation. *Cem. Concr. Res.* **1997**, *27*, 1581–1590.

852 (19) Pellenq, R. J.-M.; Kushima, A.; Shahsavari, R.; Van Vliet, K. J.; Buehler, M. J.; Yip, S.; Ulm, F.-J. A
853   Realistic Molecular Model of Cement Hydrates. *Proc. Natl. Acad. Sci.* **2009**, *106*, 16102–16107.

854 (20) Richardson, I. G. The Importance of Proper Crystal-Chemical and Geometrical Reasoning
855   Demonstrated Using Layered Single and Double Hydroxides Research Papers. **2013**, 150–162.

856 (21) Abdolhosseini Qomi, M.; Krakowiak, K. J.; Bauchy, M.; Stewart, K. L.; Shahsavari, R.; Jagannathan,
857   D.; Brommer, D. B.; Baronnet, A.; Buehler, M. J.; Yip, S.; et al. Combinatorial Molecular
858   Optimization of Cement Hydrates. *Nat. Commun.* **2014**, *5*, 4960.

859 (22) Kovačević, G.; Persson, B.; Nicoleau, L.; Nonat, A.; Veryazov, V. Atomistic Modeling of Crystal
860   Structure of Ca1.67SiHx. *Cem. Concr. Res.* **2015**, *67*, 197–203.

861 (23) Kovačević, G.; Nicoleau, L.; Nonat, A.; Veryazov, V. Revised Atomistic Models of the Crystal
862   Structure of C-S-H with High C/S Ratio. *Zeitschrift für Phys. Chemie* **2016**, *230*, 1411–1424.

863 (24) Androniuk, I. Effects of Cement Organic Additives on the Adsorption of Uranyl Ions on Calcium
864   Silicate Hydrate Phases : Experimental Determination and Computational Molecular Modelling,
865   Ecole nationale supérieure Mines-Télécom Atlantique, Nantes, 2017.

866 (25) Androniuk, I.; Landesman, C.; Henocq, P.; Kalinichev, A. G. Adsorption of Gluconate and Uranyl
867   on C-S-H Phases: Combination of Wet Chemistry Experiments and Molecular Dynamics
868   Simulations for the Binary Systems. *Phys. Chem. Earth* **2017**, *99*, 194–203.

869 (26) Androniuk, I.; Kalinichev, A. G. Molecular Dynamics Simulation of the Interaction of Uranium
870   (VI) with the C–S–H Phase of Cement in the Presence of Gluconate. *Appl. Geochemistry* **2020**,
871   *113*, 104496.

872 (27) Grangeon, S.; Claret, F.; Linard, Y.; Chiaberge, C. X-Ray Diffraction: A Powerful Tool to Probe and
873   Understand the Structure of Nanocrystalline Calcium Silicate Hydrates. *Acta Crystallogr. Sect. B*
874   *Struct. Sci. Cryst. Eng. Mater.* **2013**, *69*, 465–473.

875 (28) Bauchy, M.; Qomi, M. J. A.; Ulm, F. J.; Pellenq, R. J. M. Order and Disorder in Calcium-Silicate-
876   Hydrate. *J. Chem. Phys.* **2014**, *140*.

877 (29) Soyer-Uzun, S.; Chae, S. R.; Benmore, C. J.; Wenk, H. R.; Monteiro, P. J. M. Compositional Evolution
878   of Calcium Silicate Hydrate (C-S-H) Structures by Total X-Ray Scattering. *J. Am. Ceram. Soc.*
879   **2012**, *95*, 793–798.

880 (30) Meral, C.; Benmore, C. J.; Monteiro, P. J. M. The Study of Disorder and Nanocrystallinity in C-S-H,
881   Supplementary Cementitious Materials and Geopolymers Using Pair Distribution Function
882   Analysis. *Cem. Concr. Res.* **2011**, *41*, 696–710.

883 (31) Cuesta, A.; Santacruz, I.; De la Torre, A. G.; Dapiaggi, M.; Zea-Garcia, J. D.; Aranda, M. A. G. Local
884   Structure and Ca/Si Ratio in C-S-H Gels from Hydration of Blends of Tricalcium Silicate and
885   Silica Fume. *Cem. Concr. Res.* **2021**, *143*, 106405.

886 (32) Kunhi Mohamed, A.; Moutzouri, P.; Berruyer, P.; Walder, B. J.; Siramanont, J.; Harris, M.; Negroni,
887   M.; Galmarini, S. C.; Parker, S. C.; Scrivener, K. L.; et al. The Atomic-Level Structure of
888   Cementitious Calcium Aluminate Silicate Hydrate. *J. Am. Chem. Soc.* **2020**, *142*, 11060–11071.

889 (33) Wittmann, F. H. Interaction of Hardened Cement Paste and Water. *J. Am. Ceram. Soc.* **1973**, *56*,
890   409–415.

891 (34) Sun, E. W. H.; Bourg, I. C. Molecular Dynamics Simulations of Mineral Surface Wettability by
892   Water versus CO_2: Thin Films, Contact Angles, and Capillary Pressure in a Silica Nanopore. *J.*
893   *Phys. Chem. C* **2020**, *124*, 25382–25395.

894 (35) Schneider, M.; Maurath, J.; Fischer, S. B.; Weiß, M.; Willenbacher, N.; Koos, E. Suppressing Crack
895   Formation in Particulate Systems by Utilizing Capillary Forces. *ACS Appl. Mater. Interfaces* **2017**,
896   *9*, 11095–11105.

897 (36) Sinko, R.; Bažant, Z. P.; Keten, S. A Nanoscale Perspective on the Effects of Transverse
898   Microprestress on Drying Creep of Nanoporous Solids. *Proc. R. Soc. A Math. Phys. Eng. Sci.* **2018**,
899   *474*.

900 (37) Zhang, D.; Ghouleh, Z.; Shao, Y. Review on Carbonation Curing of Cement-Based Materials. *J. CO2*
901   *Util.* **2017**, *21*, 119–131.

902 (38) Jönsson, B.; Nonat, A.; Labbez, C.; Cabane, B.; Wennerström, H. Controlling the Cohesion of
903   Cement Paste. *Langmuir* **2005**, *21*, 9211–9221.

904 (39) Bonnaud, P. A.; Ji, Q.; Coasne, B.; Pellenq, R. J. M.; Van Vliet, K. J. Thermodynamics of Water
905   Confined in Porous Calcium-Silicate-Hydrates. *Langmuir* **2012**, *28*, 11422–11432.

906 (40) Manzano, H.; Moeini, S.; Marinelli, F.; van Duin, A. C. T.; Ulm, F.-J.; Pellenq, R. J.-M. Confined
907   Water Dissociation in Microporous Defective Silicates: Mechanism, Dipole Distribution, and

908   Impact on Substrate Properties. *J. Am. Chem. Soc.* **2012**, *134*, 2208–2215.

909 (41) Zhou, T.; Ioannidou, K.; Ulm, F.-J.; Bazant, M. Z.; Pellenq, R. J. M. Multiscale Poromechanics of Wet
910   Cement Paste. *Proc. Natl. Acad. Sci.* **2019**, *116*, 10652–10657.

911 (42) Ferraris, C. F.; Wittmann, F. H. Shrinkage Mechanisms of Hardened Cement Paste. *Cem. Concr.*
912   *Res.* **1987**, *17*, 453–464.

913 (43) Vandamme, M.; Ulm, F.-J. Nanogranular Origin of Concrete Creep. *Proc. Natl. Acad. Sci.* **2009**,
914   *106*, 10552–10557.

915 (44) Powers, T. C.; Brownyard, T. L. Studies of the Physical Properties of Hardened Portland Cement
916   Paste. *ACI J. Proc.* **1946**, *43*, 249–336.

917 (45) Allen, A. J.; Thomas, J. J.; Jennings, H. M. Composition and Density of Nanoscale Calcium-Silicate-
918   Hydrate in Cement. *Nat. Mater.* **2007**, *6*, 311–316.

919 (46) Pinson, M. B.; Masoero, E.; Bonnaud, P. A.; Thomas, J. J.; Bazant, M. Z. Hysteresis from Multiscale
920   Porosity : Modeling Water Sorption and Shrinkage in Cement Paste. *Phys. Rev. Appl.* **2015**, *3*,
921   064009–066016.

922 (47) Maruyama, I.; Ohkubo, T.; Haji, T.; Kurihara, R. Dynamic Microstructural Evolution of Hardened
923   Cement Paste during First Drying Monitored by 1H NMR Relaxometry. *Cem. Concr. Res.* **2019**,
924   *122*, 107–117.

925 (48) McDonald, P. J.; Rodin, V.; Valori, A. Characterisation of Intra- and Inter-C–S–H Gel Pore Water in
926   White Cement Based on an Analysis of NMR Signal Amplitudes as a Function of Water Content.
927   *Cem. Concr. Res.* **2010**, *40*, 1656–1663.

928 (49) Muller, A. C. A.; Scrivener, K. L.; Gajewicz, A. M.; McDonald, P. J. Use of Bench-Top NMR to
929   Measure the Density , Composition and Desorption Isotherm of C-S-H in Cement Paste.
930   *Microporous Mesoporous Mater.* **2013**, *178*, 99–103.

931 (50) Valori, A.; McDonald, P. J.; Scrivener, K. L. The Morphology of C-S-H: Lessons from 1H Nuclear
932   Magnetic Resonance Relaxometry. *Cem. Concr. Res.* **2013**, *49*, 65–81.

933 (51) Roosz, C.; Gaboreau, S.; Grangeon, S.; Prêt, D.; Montouillout, V.; Maubec, N.; Ory, S.; Blanc, P.;
934   Vieillard, P.; Henocq, P. Distribution of Water in Synthetic Calcium Silicate Hydrates. *Langmuir*
935   **2016**, *32*, 6794–6805.

936 (52) Youssef, M.; Pellenq, R. J. M.; Yildiz, B. Glassy Nature of Water in an Ultraconfining Disordered
937   Material: The Case of Calcium-Silicate-Hydrate. *J. Am. Chem. Soc.* **2011**, *133*, 2499–2510.

938 (53) Soper, A. K. Joint Structure Refinement of X-Ray and Neutron Diffraction Data on Disordered
939   Materials: Application to Liquid Water. *J. Phys. Condens. Matter* **2007**, *19*.

940 (54) Qomi, M. J. A.; Bauchy, M.; Ulm, F. J.; Pellenq, R. J. M. Anomalous Composition-Dependent
941   Dynamics of Nanoconfined Water in the Interlayer of Disordered Calcium-Silicates. *J. Chem.*
942   *Phys.* **2014**, *140*, 054515.

943 (55) Bourg, I. C.; Steefel, C. I. Molecular Dynamics Simulations of Water Structure and Diffusion in
944   Silica Nanopores. *J. Phys. Chem. C* **2012**, *116*, 11556–11564.

945 (56) Wang, J.; Kalinichev, A. G.; Kirkpatrick, R. J.; Cygan, R. T. Structure, Energetics, and Dynamics of
946   Water Adsorbed on the Muscovite (001) Surface: A Molecular Dynamics Simulation. *J. Phys.*
947   *Chem. B* **2005**, *109*, 15893–15905.

948 (57) Schoonheydt, R. A.; Johnston, C. T.; Bergaya, F. *Clay Minerals and Their Surfaces*; Elsevier:
949   Amsterdam, Netherlands, 2018; Vol. 9, pp 1-21.

950 (58) Johnston, C. T. *Clay Mineral–Water Interactions*; Schoonheydt, R; Johnston, C T; Bergaya, F., Ed.;
951   Elsevier: Amsterdam, Netherlands, 2018; Vol. 9, pp 89-124 .

952 (59) Marry, V.; Turq, P. Structure and Dynamics of Water at a Clay Surface from Molecular Dynamics
953 Simulation. *Phys. Chem. Chem. Phys.* **2008**, *10*, 4802–4813.

954 (60) Puibasset, J.; Pellenq, R. J.-M. Water Adsorption in Disordered Mesoporous Silica (Vycor) at 300
955 K and 650 K: A Grand Canonical Monte Carlo Simulation Study of Hysteresis. *J. Chem. Phys.*
956 **2005**, *122*, 94704.

957 (61) Pezzotti, S.; Havenith, M.; Gaigeot, M. P.; Serva, A.; Sebastiani, F.; Brigiano, F. S.; Galimberti, D. R.;
958 Potier, L.; Alfarano, S.; Schwaab, G. Molecular Fingerprints of Hydrophobicity at Aqueous
959 Interfaces from Theory and Vibrational Spectroscopies. *J. Phys. Chem. Lett.* **2021**, *12*, 3827–
960 3836.

961 (62) Fischer, H. E.; Barnes, A. C.; Salmon, P. S. Neutron and X-Ray Diffraction Studies of Liquids and
962 Glasses. *Reports Prog. Phys.* **2006**, *69*, 233–299.

963 (63) Cuello, G. J. Structure Factor Determination of Amorphous Materials by Neutron Diffraction. *J.*
964 *Phys. Condens. Matter* **2008**, *20*, 244109.

965 (64) Pitteloud, C.; Hugh Powell, D.; Soper, A. K.; Benmore, C. J. Structure of Interlayer Water in
966 Wyoming Montmorillonite Studied by Neutron Diffraction with Isotopic Substitution. *Phys. B*
967 *Condens. Matter* **2000**, *276–278*, 236–237.

968 (65) Powell, D. H.; Fischer, H. E.; Skipper, N. T. The Structure of Interlayer Water in Li-
969 Montmorillonite Studied by Neutron Diffraction with Isotopic Substitution. *J. Phys. Chem. B*
970 **1998**, *102*, 10899–10905.

971 (66) Skipper, N. T.; Soper, A. K.; McConnell, J. D. C. The Structure of Interlayer Water in Vermiculite. *J.*
972 *Chem. Phys.* **1991**, *94*, 5751–5760.

973 (67) Masoumi, S.; Zare, S.; Valipour, H.; Abdolhosseini Qomi, M. J. Effective Interactions between
974 Calcium-Silicate-Hydrate Nanolayers. *J. Phys. Chem. C* **2019**, *123*, 4755–4766.

975 (68) Haas, J.; Nonat, A. From C-S-H to C-A-S-H: Experimental Study and Thermodynamic Modelling.
976 *Cem. Concr. Res.* **2015**, *68*, 124–138.

977 (69) Brunauer, S.; Emmett, P. H.; Teller, E. Adsorption of Gases in Multimolecular Layers. *J. Am. Chem.*
978 *Soc.* **1938**, *60*, 309–319.

979 (70) Hagymassy, J.; Brunauer, S.; Mikhail, R. S. Pore Structure Analysis by Water Vapor Adsorption: I.
980 t-Curves for Water Vapor. *J. Colloid Interface Sci.* **1969**, *29*, 485–491.

981 (71) Kieffer, J.; Wright, J. P. PyFAI: A Python Library for High Performance Azimuthal Integration on
982 GPU. *Powder Diffr.* **2013**, *28*, S339–S350.

983 (72) Juhás, P.; Davis, T.; Farrow, C. L.; Billinge, S. J. L. PDFgetX3 : A Rapid and Highly Automatable
984 Program for Processing Powder Diffraction Data into Total Scattering Pair Distribution
985 Functions. *J. Appl. Crystallogr.* **2013**, *46*, 560–566.

986 (73) Toby, B. H.; Dreele, R. B. Von. GSAS-II : The Genesis of a Modern Open-Source All Purpose
987 Crystallography Software Package. **2013**, 544–549.

988 (74) Fischer, H. E.; Cuello, G. J.; Palleau, P.; Feltin, D.; Barnes, A. C.; Badyal, Y. S.; Simonson, J. M. D4c: A
989 Very High Precision Diffractometer for Disordered Materials. *Appl. Phys. A* **2002**, *74*, s160–s162.

990 (75) Howe, M. A.; McGreevy, R. L.; Zetterstrom, P. CORRECT: A Correction Programme for Neutron
991 Diffraction Data. *NFL Studsvik Intern. Rep.* **1998**.

992 (76) Sears, V. F. Neutron Scattering Lengths and Cross Sections. *Neutron News* **1992**, *3*, 26–37.

993 (77) Lorch, E. Neutron Diffraction by Germania, Silica and Radiation-Damaged Silica Glasses. *J. Phys.*
994 *C Solid State Phys.* **1969**, *2*, 229–237.

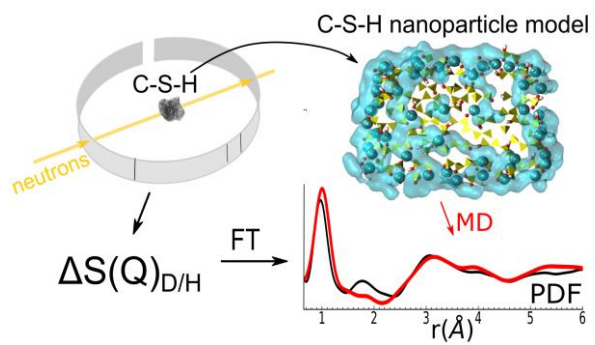995 (78) Soper, A. K. GudrunN and GudrunX Programs for Correcting Raw Neutron and X-Ray Total

996   Scattering Data to Differential Cross Section. RAL Library: Didcot, U.K. 2011.

997   (79) Plimpton, S. Fast Parallel Algorithms for Short-Range Molecular Dynamics. *J. Comput. Phys.*
998   **1997**, *117*, 1–42.

999   (80) Berendsen, H. J. C.; Grigera, J. R.; Straatsma, T. P. The Missing Term in Effective Pair Potentials. *J.*
1000   *Phys. Chem.* **1987**, *91*, 6269–6271.

1001 (81) Cygan, R. T.; Liang, J. J.; Kalinichev, A. G. Molecular Models of Hydroxide, Oxyhydroxide, and Clay
1002   Phases and the Development of a General Force Field. *J. Phys. Chem. B* **2004**, *108*, 1255–1266.

1003 (82) Kalinichev, A. G.; Wang, J.; Kirkpatrick, R. J. Molecular Dynamics Modeling of the Structure,
1004   Dynamics and Energetics of Mineral-Water Interfaces: Application to Cement Materials. *Cem.*
1005   *Concr. Res.* **2007**, *37*, 337–347.

1006 (83) Bourg, I. C.; Sposito, G. Molecular Dynamics Simulations of the Electrical Double Layer on
1007   Smectite Surfaces Contacting Concentrated Mixed Electrolyte (NaCl-CaCl(2)) Solutions. *J. Colloid*
1008   *Interface Sci.* **2011**, *360*, 701–715.

1009 (84) Ferrage, E.; Lanson, B.; Michot, L. J.; Robert, J. L. Hydration Properties and Interlayer
1010   Organization of Water and Ions in Synthetic Na-Smectite with Tetrahedral Layer Charge. Part 1.
1011   Results from X-Ray Diffraction Profile Modeling. *J. Phys. Chem. C* **2010**, *114*, 4515–4526.

1012 (85) Ockwig, N. W.; Cygan, R. T.; Criscenti, L. J.; Nenoff, T. M. Molecular Dynamics Studies of
1013   Nanoconfined Water in Clinoptilolite and Heulandite Zeolites. *Phys. Chem. Chem. Phys.* **2008**, *10*,
1014   800–807.

1015 (86) Roscioni, O. M.; Muccioli, L.; Zannoni, C. Predicting the Conditions for Homeotropic Anchoring of
1016   Liquid Crystals at a Soft Surface. 4-n-Pentyl-4′-Cyanobiphenyl on Alkylsilane Self-Assembled
1017   Monolayers. *ACS Appl. Mater. Interfaces* **2017**, *9*, 11993–12002.

1018 (87) Fernandez-Martinez, A.; Tao, J.; Wallace, A. F.; Bourg, I. C.; Johnson, M. R.; De Yoreo, J. J.; Sposito,
1019   G.; Cuello, G. J.; Charlet, L. Curvature-Induced Hydrophobicity at Imogolite-Water Interfaces.
1020   *Environ. Sci. Nano* **2020**, *7*, 2759–2772.

1021 (88) Skelton, A. A.; Fenter, P.; Kubicki, J. D.; Wesolowski, D. J.; Cummings, P. T. Simulations of the
1022   Quartz(1011)/Water Interface: A Comparison of Classical Force Fields, Ab Initio Molecular
1023   Dynamics, and X-Ray Reflectivity Experiments. *J. Phys. Chem. C* **2011**, *115*, 2076–2088.

1024 (89) Ferrage, E.; Sakharov, B. A.; Michot, L. J.; Delville, A.; Bauer, A.; Lanson, B.; Grangeon, S.; Frapper,
1025   G.; Jiménez-Ruiz, M.; Cuello, G. J. Hydration Properties and Interlayer Organization of Water and
1026   Ions in Synthetic Na-Smectite with Tetrahedral Layer Charge. Part 2. Toward a Precise Coupling
1027   between Molecular Simulations and Diffraction Data. *J. Phys. Chem. C* **2011**, *115*, 1867–1881.

1028 (90) Wander, M. C. F.; Clark, A. E. Structural and Dielectric Properties of Quartz - Water Interfaces. *J.*
1029   *Phys. Chem. C* **2008**, *112*, 19986–19994.

1030 (91) Underwood, T. R.; Bourg, I. C. Large-Scale Molecular Dynamics Simulation of the Dehydration of
1031   a Suspension of Smectite Clay Nanoparticles. *J. Phys. Chem. C* **2020**, *124*, 3702–3714.

1032 (92) Kalinichev, A. G.; Kirkpatrick, R. J. Molecular Dynamics Modeling of Chloride Binding to the
1033   Surfaces of Calcium Hydroxide, Hydrated Calcium Aluminate, and Calcium Silicate Phases. *Chem.*
1034   *Mater.* **2002**, *14*, 3539–3549.

1035 (93) Shahsavari, R.; Pellenq, R. J. M.; Ulm, F. J. Empirical Force Fields for Complex Hydrated Calcio-
1036   Silicate Layered Materials. *Phys. Chem. Chem. Phys.* **2011**, *13*, 1002–1011.

1037 (94) Mishra, R. K.; Mohamed, A. K.; Geissbühler, D.; Manzano, H.; Jamil, T.; Shahsavari, R.; Kalinichev,
1038   A. G.; Galmarini, S.; Tao, L.; Heinz, H.; Pellenq, R.; van Duin, A. C. T.; Parker, S. C.; Flatt, R. J.;
1039   Bowen, P. Cemff: A Force Field Database for Cementitious Materials Including Validations,
1040   Applications and Opportunities. *Cem. Concr. Res.* **2017**, *102*, 68–89.

(95) Van Duin, A. C. T.; Dasgupta, S.; Lorant, F.; Goddard, W. A. ReaxFF: A Reactive Force Field for Hydrocarbons. *J. Phys. Chem. A* **2001**, *105*, 9396–9409.

(96) Lammers, L. N.; Bourg, I. C.; Okumura, M.; Kolluri, K.; Sposito, G.; Machida, M. Molecular Dynamics Simulations of Cesium Adsorption on Illite Nanoparticles. *J. Colloid Interface Sci.* **2017**, *490*, 608–620.

(97) Bonaccorsi, E.; Merlino, S.; Kampf, A. R. The Crystal Structure of Tobermorite 14 Å (Plombierite), a C-S-H Phase. *J. Am. Ceram. Soc.* **2005**, *88*, 505–512.

(98) Heinz, H.; Lin, T. J.; Kishore Mishra, R.; Emami, F. S. Thermodynamically Consistent Force Fields for the Assembly of Inorganic, Organic, and Biological Nanostructures: The INTERFACE Force Field. *Langmuir* **2013**, *29*, 1754–1765.

(99) Machesky, M. L.; Předota, M.; Wesolowski, D. J.; Vlcek, L.; Cummings, P. T.; Rosenqvist, J.; Ridley, M. K.; Kubicki, J. D.; Bandura, A. V.; Kumar, N.; et al. Surface Protonation at the Rutile (110) Interface: Explicit Incorporation of Solvation Structure within the Refined MUSIC Model Framework. *Langmuir* **2008**, *24*, 12331–12339.

(100) Tournassat, C.; Bourg, I. C.; Holmboe, M.; Sposito, G.; Steefel, C. I. Molecular Dynamics Simulations of Anion Exclusion in Clay Interlayer Nanopores. *Clays Clay Miner.* **2016**, *64*, 374–388.

(101) Collin, M.; Gin, S.; Dazas, B.; Mahadevan, T.; Du, J.; Bourg, I. C. Molecular Dynamics Simulations of Water Structure and Diffusion in a 1 Nm Diameter Silica Nanopore as a Function of Surface Charge and Alkali Metal Counterion Identity. *J. Phys. Chem. C* **2018**, *122*, 17764–17776.

(102) Cong, X.; Kirkpatrick, R. J. 1H — 29Si CPMAS NMR Study of the Structure of Calcium Silicate Hydrate. *Adv. Cem. Res.* **1995**, *7*, 103–111.

(103) Brunet, F.; Bertani, P.; Charpentier, T.; Nonat, A.; Virlet, J. Application of 29 Si Homonuclear and 1 H-29 Si Heteronuclear NMR Correlation to Structural Studies of Calcium Silicate Hydrates. *J. Phys. Chem. B* **2004**, *108*, 15494–15502.

(104) Rodriguez, E. T.; Richardson, I. G.; Black, L.; Boehm-Courjault, E.; Nonat, A.; Skibsted, J. Composition, Silicate Anion Structure and Morphology of Calcium Silicate Hydrates (C-S-H) Synthesised by Silica-Lime Reaction and by Controlled Hydration of Tricalcium Silicate (C3S). *Adv. Appl. Ceram.* **2015**, *114*, 362–371.

(105) Richardson, I. G. The Calcium Silicate Hydrates. *Cem. Concr. Res.* **2008**, *38*, 137–158.

(106) Feldman, R. F.; Sereda, P. J. A New Model for Hydrated Portland Cement and Its Practical Implications. *Eng. J.* **1970**, *53*, 53–59.

(107) Yu, P.; Kirkpatrick, R. Thermal Dehydration of Tobermorite and Jennite. *Concr. Sci. Eng.* **1999**, *1*, 185–191.

(108) Jansen, D.; Naber, C.; Ectors, D.; Lu, Z.; Kong, X.-M.; Goetz-Neunhoeffer, F.; Neubauer, J. The Early Hydration of OPC Investigated by In-Situ XRD, Heat Flow Calorimetry, Pore Water Analysis and 1H NMR: Learning about Adsorbed Ions from a Complete Mass Balance Approach. *Cem. Concr. Res.* **2018**, *109*, 230–242.

(109) Sing, K. S. W. Reporting Physisorption Data for Gas/Solid Systems with Special Reference to the Determination of Surface Area and Porosity (Recommendations 1984). *Pure Appl. Chem.* **1985**, *57*, 603–619.

(110) L'Hôpital, E.; Lothenbach, B.; Kulik, D. A.; Scrivener, K. Influence of Calcium to Silica Ratio on Aluminium Uptake in Calcium Silicate Hydrate. *Cem. Concr. Res.* **2016**, *85*, 111–121.

(111) Renaudin, G.; Russias, J.; Leroux, F.; Frizon, F.; Cau-dit-Coumes, C. Structural Characterization of C-S-H and C-A-S-H Samples-Part I: Long-Range Order Investigated by Rietveld Analyses. *J. Solid*

1086   *State Chem.* **2009**, *182*, 3312–3319.

(112)   Beaudoin, J.; Odler, I. *Hydration, Setting and Hardening of Portland Cement*, 5th ed.; Hewlett, P., Liska, M., Eds.; Elsevier Ltd.: Oxford, U.K., 2019.

(113)   Fujii, K.; Kondo, W. Heterogeneous Equilibrium of Calcium Silicate Hydrate in Water at 30 °C. *J. Chem. Soc. Dalt. Trans.* **1981**, No. 2, 645–651.

(114)   Nemes, N. M.; Neumann, D. A.; Livingston, R. A. States of Water in Hydrated C3S (Tricalcium Silicate) as a Function of Relative Humidity. *J. Mater. Res.* **2006**, *21*, 2516–2523.

(115)   Odler, I. The BET-Specific Surface Area of Hydrated Portland Cement and Related Materials. **2003**, *33*, 2049–2056.

(116)   Gaboreau, S.; Grangeon, S.; Claret, F.; Ihiawakrim, D.; Ersen, O.; Montouillout, V.; Maubec, N.; Roosz, C.; Henocq, P.; Carteret, C. Hydration Properties and Interlayer Organization in Synthetic C-S-H. *Langmuir* **2020**, *36*, 9449–9464.

(117)   Richardson, I. G. Tobermorite/Jennite- and Tobermorite/Calcium Hydroxide-Based Models for the Structure of C-S-H: Applicability to Hardened Pastes of Tricalcium Silicate, β-Dicalcium Silicate, Portland Cement, and Blends of Portland Cement with Blast-Furnace Slag, Metakaol. *Cem. Concr. Res.* **2004**, *34*, 1733–1777.

(118)   Bauchy, M.; Laubie, H.; Abdolhosseini Qomi, M. J.; Hoover, C. G.; Ulm, F. J.; Pellenq, R. J. M. Fracture Toughness of Calcium-Silicate-Hydrate from Molecular Dynamics Simulations. *J. Non. Cryst. Solids* **2015**, *419*, 58–64.

(119)   Senftle, T. P.; Hong, S.; Islam, M. M.; Kylasa, S. B.; Zheng, Y.; Shin, Y. K.; Junkermeier, C.; Engel-Herbert, R.; Janik, M. J.; Aktulga, H. M.; et al. The ReaxFF Reactive Force-Field: Development, Applications and Future Directions. *npj Comput. Mater.* **2016**, *2*, 15011.

(120)   Heinz, H.; Koerner, H.; Anderson, K. L.; Vaia, R. A.; Farmer, B. L. Force Field for Mica-Type Silicates and Dynamics of Octadecylammonium Chains Grafted to Montmorillonite. *Chem. Mater.* **2005**, *17*, 5658–5669.

(121)   Jiménez-Ruiz, M.; Ferrage, E.; Blanchard, M.; Fernandez-Castanon, J.; Delville, A.; Johnson, M. R.; Michot, L. J. Combination of Inelastic Neutron Scattering Experiments and Ab Initio Quantum Calculations for the Study of the Hydration Properties of Oriented Saponites. *J. Phys. Chem. C* **2017**, *121*, 5029–5040.

(122)   Banfield, J. F.; Zhang, H. Nanoparticles in the Environment. *Rev. Mineral. Geochemistry* **2001**, *44*, 1–58.

(123)   Ohtaki, H.; Radnai, T. Structure and Dynamics of Hydrated Ions. *Chem. Rev.* **1993**, *93*, 1157–1204.

(124)   Loganathan, N.; Yazaydin, A. O.; Bowers, G. M.; Kalinichev, A. G.; Kirkpatrick, R. J. Cation and Water Structure, Dynamics, and Energetics in Smectite Clays: A Molecular Dynamics Study of Ca-Hectorite. *J. Phys. Chem. C* **2016**, *120*, 12429–12439.

(125)   Bonnaud, P. A.; Coasne, B.; Pellenq, R. J. M. Solvated Calcium Ions in Charged Silica Nanopores. *J. Chem. Phys.* **2012**, *137*.

(126)   Marcus, Y. Ionic Radii in Aqueous Solutions. *Chem. Rev.* **1988**, *88*, 1475–1498.

(127)   Gilbert, B.; Lin, Z.; Goodell, C.; Zhang, H.; Banfield, J. Surface Chemistry Controls Crystallinity of ZnS Nanoparticles. *Nano Lett.* **2006**, *6*, 605–610.

1127 **TOC GRAPHIC**

1128